Research Square

Preprints are preliminary reports that have not undergone peer review.
They should not be considered conclusive, used to inform clinical practice,
or referenced by the media as validated information.

Chaotic Dynamics of Clifford Attractors and its Application in Economics

HIMANSHU BARANWAL

ma20d202@smail.iitm.ac.in

Indian Institute of Technology Madras

Shubham Maurya

Indian Institute of Technology Madras

Sishu Shankar Muni

Indian Institute of Information Technology and Management, Kerala

A. K. B. Chand

Indian Institute of Technology Madras

Research Article

Keywords: Clifford attractor, bifurcation, Lyapunov exponents, 0–1 test, fixed point, stability, time series

Posted Date: September 9th, 2026

DOI: https://doi.org/10.21203/rs.3.rs-10963890/v1

License: This work is licensed under a Creative Commons Attribution 4.0 International License.
Read Full License

Additional Declarations: The authors declare no competing interests.

Chaotic Dynamics of Clifford Attractors and its Application in Economics

S. Maurya [1], H. Baranwal [2*] Sishu Shankar Muni [3], A. K. B. Chand [4]

[1]Department of Mathematics, Indian Institute of Technology Madras, Chennai - 600036, India;
ma18c035@alumni.iitm.ac.in

[2] Department of Mathematics, Indian Institute of Technology Madras, Chennai - 600036, India;
ma20d202@smail.iitm.ac.in

[3]School of Digital Sciences, Digital University Kerala, Pallipuram-695317, Kerala, India
sishushankarmuni@gmail.com

[4] Department of Mathematics, Indian Institute of Technology Madras, Chennai - 600036, India;
chand@iitm.ac.in

*Corresponding Author (ma20d202@smail.iitm.ac.in)

Abstract

This paper presents a comprehensive dynamical analysis of the Clifford attractor, a two-dimensional discrete-time chaotic system governed by the equations $x_{n+1} = \sin(ay_n) + c\cos(ax_n)$ and $y_{n+1} = \sin(bx_n) + d\cos(by_n)$. We investigate the behavior of the system by sequential single-parameter sweeps, varying $(a, b, c,$ and $d)$ independently, using multiple complementary analytical techniques. Bifurcation diagrams are constructed for each parameter, revealing period-doubling cascade routes to chaos, such as from deep negative to high positive chaos, periodic windows, transitional behavior, and crisis events. The system's sensitivity to initial conditions is quantified through an infinitesimal initial separation using the Largest Lyapunov Exponent, confirming chaotic behavior for canonical parameter sets. The 0–1 test for chaos is employed as a purely statistical binary diagnostic verifying tool. Fixed point analysis identifies equilibrium through stability analysis, phase portrait, basin of attraction, and eigenvalue analysis. It is shown that the system can exhibit rich dynamical behaviors such as stable to chaos, multistability, coexistence, and fractal structure. These behaviors are measured and visualized by seven distinct entropies, fractal dimension, correlation dimension, and forward-backward continuation bifurcation diagrams. Beyond theoretical characterization, we demonstrate novel applications of the Clifford attractor in market Economics. The attractor's rich dynamical repertoire and sensitivity to parameter variations make it particularly suitable for these applications. Our results establish the Clifford attractor as both a theoretically rich dynamical system and a practical tool for modern economic challenges.

Mathematics Subject Classification— Primary 37D45, 37D60; Secondary 37C70, 37D40, 37N35, 28A80.
Keywords— Clifford attractor, bifurcation, Lyapunov exponents, 0–1 test, fixed point, stability, time series.

1 Introduction

The increasing risk of confidential data breaches in modern digital communication systems makes it necessary for us to develop robust encryption methods [4]. As day by day the use and transmission of text and image data increases, this data becomes vulnerable to interception and unauthorized access [15]. In this context, chaos-based cryptographic methods have gained significant attention because of their intrinsic properties, which include sensitivity to initial conditions, ergodicity, unpredictability, and strong pseudo-random behavior [37, 21].

For secure data transmission, chaotic maps and strange attractors have been widely explored. Similarly, the Clifford attractor shows considerable potential in cryptographic applications. Ivanova et al. [16] proposed a symmetric text encryption algorithm based on two Clifford attractors combined with a novel pseudo-random byte generation process. Their study reported high entropy values and near-zero correlation coefficients; it confirms that for secure encryption, the Clifford attractor can generate sequences with strong statistical properties.

In the context of image encryption, Kanafchian and Fathi-Vajargah [17] introduced a novel scheme combining the Clifford attractor with a noisy logistic map for secure naval image transmission. Their approach employed chaotic permutation and diffusion mechanisms and demonstrated strong resistance against statistical and differential attacks.

Furthermore, An RGB image encryption algorithm (proposed by El Azzaby et al. [1]) is based on the combination of the Clifford attractor, bilinear transformations, and XOR masking. Their method generated multiple substitution boxes derived from the attractor dynamics to independently encrypt the red, green, and blue channels. Experimental evaluations, including histogram analysis, entropy measurement, correlation coefficients, and resistance to differential attacks, confirm the robustness and effectiveness of their scheme. In a parallel development, Nardo et al. [24] proposed an alternative image encryption method that exploits the finite-precision errors inherent in digital implementations of chaotic systems. Rather than mitigating these errors as a degradation of chaotic properties, their technique harnesses the lower bound error from two natural interval extensions of the same chaotic system, Chua's circuit, to generate pseudo-random keystreams that pass the NIST statistical test suite, thereby turning a computational limitation into a source of cryptographic randomness.

These studies highlight the practical relevance of the Clifford attractor in modern cryptographic design. Because of this high level of promising experimental performance in encryption frameworks, we need to perform a deeper theoretical investigation of the dynamical properties of the Clifford attractor.

These considerations motivated us, and in this paper, we have investigated the dynamical behavior of the Clifford attractor through bifurcation analysis, Lyapunov exponents, the $0-1$ test, fixed point stability, the basin of attraction, and many more complementary nonlinear diagnostics. Our objective is to identify parameter regimes exhibiting stable chaotic behavior that are suitable for secure cryptographic implementation, which provides a solid theoretical foundation for Clifford-based encryption schemes.

The Clifford attractor, first described by Clifford Pickover (also referred to as the Pickover attractor) [28], is defined by the discrete-time system

$$\begin{aligned} x_{n+1} &= \sin(a\, y_n) + c\cos(a\, x_n), \\ y_{n+1} &= \sin(b\, x_n) + d\cos(b\, y_n), \end{aligned} \tag{1}$$

where a, b, c, and d are real-valued control parameters. Introduced in *Chaos in Wonderland* [28], this attractor serves as a compact yet dynamically rich model for studying nonlinear and chaotic behavior.

The remainder of this paper is organized as follows. Section 2 presents a detailed bifurcation analysis of the Clifford map, illustrating the transitions between periodic and chaotic regimes as control parameters vary. Section 3 studies how variations in the control parameters influence the Lyapunov exponent spectrum, thereby revealing transitions from stable dynamics to chaotic behavior. Section 4 applies the 0–1 test for chaos to independently validate the presence of regular and chaotic dynamics. Section 5 examines the fixed points of the Clifford map and their local dynamical behavior through iterative phase-space trajectories, highlighting convergence to stable equilibria and the emergence of chaotic invariant sets. Section 6 presents phase portraits to visualize the geometric evolution of trajectories and to highlight dynamical transitions between periodic orbits and strange attractors. Section 7 studies the global stability structure through basin of attraction analysis. Section 8 examines the sensitivity of the system to initial conditions, highlighting its chaotic nature. Section 9 investigates the fractal structure of the attractor and evaluates its complexity using the Kaplan–Yorke dimension. Section 10 provides an additional characterization of the system using correlation dimension analysis via the Grassberger–Procaccia method. Section 11 presents a comprehensive entropy-based analysis of the Clifford attractor over the parameter range $c \in [0.5, 2.0]$ using seven entropy measures, namely Shannon, Rẹnyi, Tsallis, Kolmogorov–Sinai, permutation, approximate, and sample entropy. This multi-entropy framework captures different aspects of dynamical complexity, including information production, statistical disorder, and nonlinear irregularity. Section 12 explores multistability, coexisting attractors, and hysteresis through parameter continuation and forward–backward sweeps. Section 13 connects the theoretical results to applications by developing a nonlinear discrete market model based on the Clifford attractor to study financial price and sentiment dynamics. Finally, Section 14 concludes the paper. Appendix A provides the complete Python source code implementation details for all analyzes conducted in this study.

2 Bifurcation structure of the proposed system

In this section, we present a bifurcation analysis of the system (1). Bifurcation analysis reveals a systematic framework for understanding qualitative changes in the system's long-term behavior as parameters are varied [7]. Also, the periodic orbit loses stability through a flip bifurcation, giving birth to a stable periodic orbit[19]. To characterize the transition from ordered to chaotic dynamics within the Clifford attractor, we perform a detailed bifurcation analysis. By keeping three of the four control parameters (a, b, c, d) constant and incrementally varying the fourth, we observe the evolution of the system's steady-state behavior. Figures 2 and 3 illustrate these transitions for the state variables x and y, respectively.

Bifurcation structure for the $x-$coordinate and varying c

We try to understand the bifurcation structure with respect to variable x and parameter c. The Clifford attractor, defined by the discrete two-dimensional system (1), exhibits a very rich bifurcation structure as c varies while other parameters remain fixed at $a = 1.5$, $b = -1.8$, and $d = 0.9$. The bifurcation diagram (Fig. 1 and Fig. 2(C)), constructed by plotting the coordinate values of x against the parameter c by sampling $c \in [-2.0, 2.0]$ at 1000 equally spaced values with the initial condition $(0.1, 0.1)$, reveals complex dynamical behaviors. Dense vertical clouds of points indicate chaotic attractors, where trajectories exhibit sensitive dependence on initial conditions and fill regions of phase space. In contrast, thin horizontal bands correspond to periodic orbits. In Fig. 2(C), for negative values of $c \leq -0.8$, the dynamical system shows fully developed chaos, which is characterized by dense point clouds spanning $x \in [-2.0, -0.8]$. The large negative coefficient amplifies the $\cos(ax_n)$ term with the opposite sign, creating strong nonlinear feedback. The system exhibits deep chaos in this region. In Fig. 2(C), in the interval $c \in [-0.8, 0]$, the system (1) exhibits chaotic behavior with a slightly reduced vertical extent compared to the deep negative regime. We can note that narrow periodic windows appear as thin vertical bands within the chaotic sea. These windows likely arise through tangent (saddle-node) bifurcations, where pairs of periodic orbits are created or destroyed. For positive $c \in [0, 0.8]$, the system again displays chaotic dynamics with an asymmetric structure caused by $b = -1.8$ and the noncommutative nature of the sine and cosine nonlinearities.

In the region $c > 1.5$, the system shows fully developed chaos (Fig. 2(C)) and complex internal structure, with visible layers or bands within the chaotic cloud that suggest the presence of unstable periodic orbits. The vertical spread increases to $x \in [1.5, 2]$, and the attractor reveals fractal geometry with intricate folding and stretching dynamics.

Periodic Windows, doubling cascade and Stability Regions

For $-0.8 \leq c \leq 1.6$, Fig. 2(C) displays broad periodic windows characterized by vertical bands, where the cloud of chaotic points collapses into a few discrete horizontal lines and the emergence of a periodic structure. These windows likely arise through

a tangent bifurcation, where a stable periodic orbit is created from the chaotic sea as c increases. Generally, we observe a hierarchical organization of periodic windows in many chaotic systems. This region exhibits a classic period-doubling cascade. The cascade begins with a stable periodic orbit (period-1 or period-2) near $c \approx 1.4$ (Fig. 1), which undergoes successive period-doubling bifurcations as c increases. Within this region, many stable zones are observed, with the most pronounced stability interval occurring for $c \in [1.18, 1.42]$. At each bifurcation point c_n, we observe that the periodic orbit loses stability through a flip bifurcation, giving birth to a stable periodic orbit. The accumulation point near $c \approx 1.55$ marks the onset of chaos following the period-doubling route.

The Period-doubling cascade in the interval $c \in [1.1, 1.5]$ (Fig. 1) provides a canonical example of a route to chaos in two-dimensional discrete maps. There are also periodic doubling cascades in different intervals that can be easily observed in Fig.2(C). Table 1 summarizes the approximate parameter values and corresponding orbit types observed in this cascade.

Table 1: Period-doubling sequence in the primary stability window.

c	Orbit Type
1.3	Period-1
1.4	Period-1
1.45	Period-2
1.5	Period-11
1.6	Chaos

Bifurcation structure for the $y-$coordinate and the remaining parameters

The system (1) , with respect to the variable x and the other parameters a, b and d, while the remaining parameters are fixed, exhibits a rich bifurcation structure. The bifurcation diagram, constructed by plotting asymptotic x-coordinate values against the parameter a (Fig. 2(A)), x-coordinate values against the parameter b (Fig. 2(B)), and x-coordinate values against the parameter d (Fig. 2(D)), reveals multiple dynamical regimes including periodic windows, period-doubling cascades, chaotic regions, and crisis phenomena.
Similarly, we see multiple dynamical regimes, including periodic windows, period-doubling cascades, chaotic regions, and crisis phenomena, by plotting asymptotic y-coordinate values against the parameters a, b, c, d (Fig. 3).
In the next section, we analyze the quantitative characterization by its spectrum of Lyapunov exponents of the system (1).

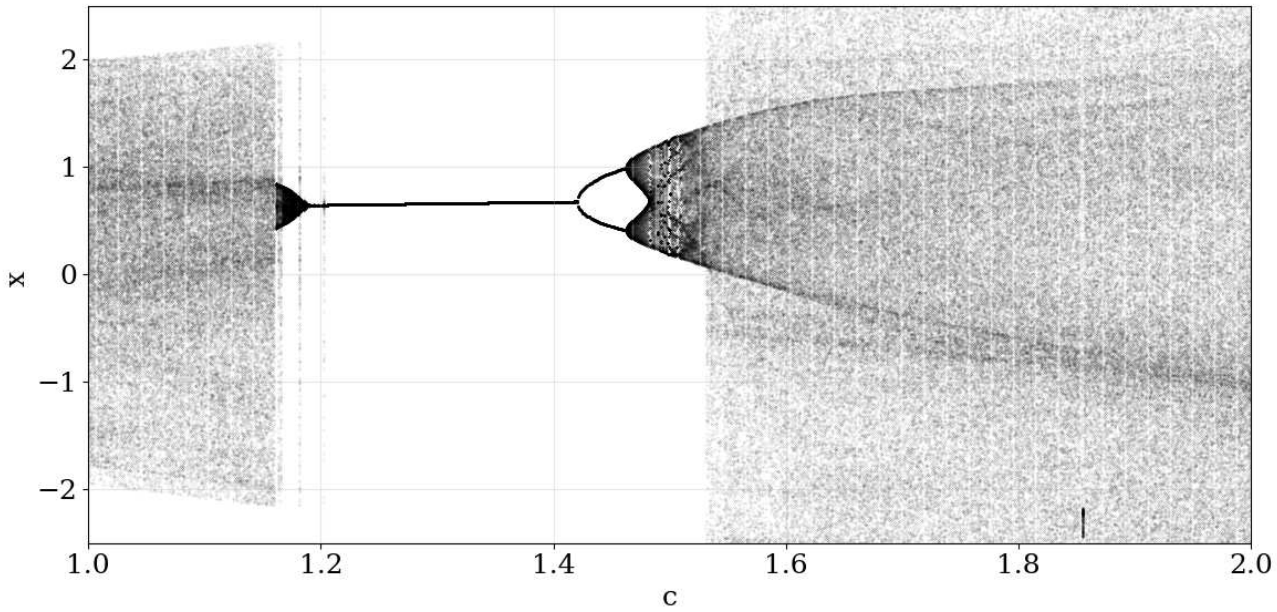
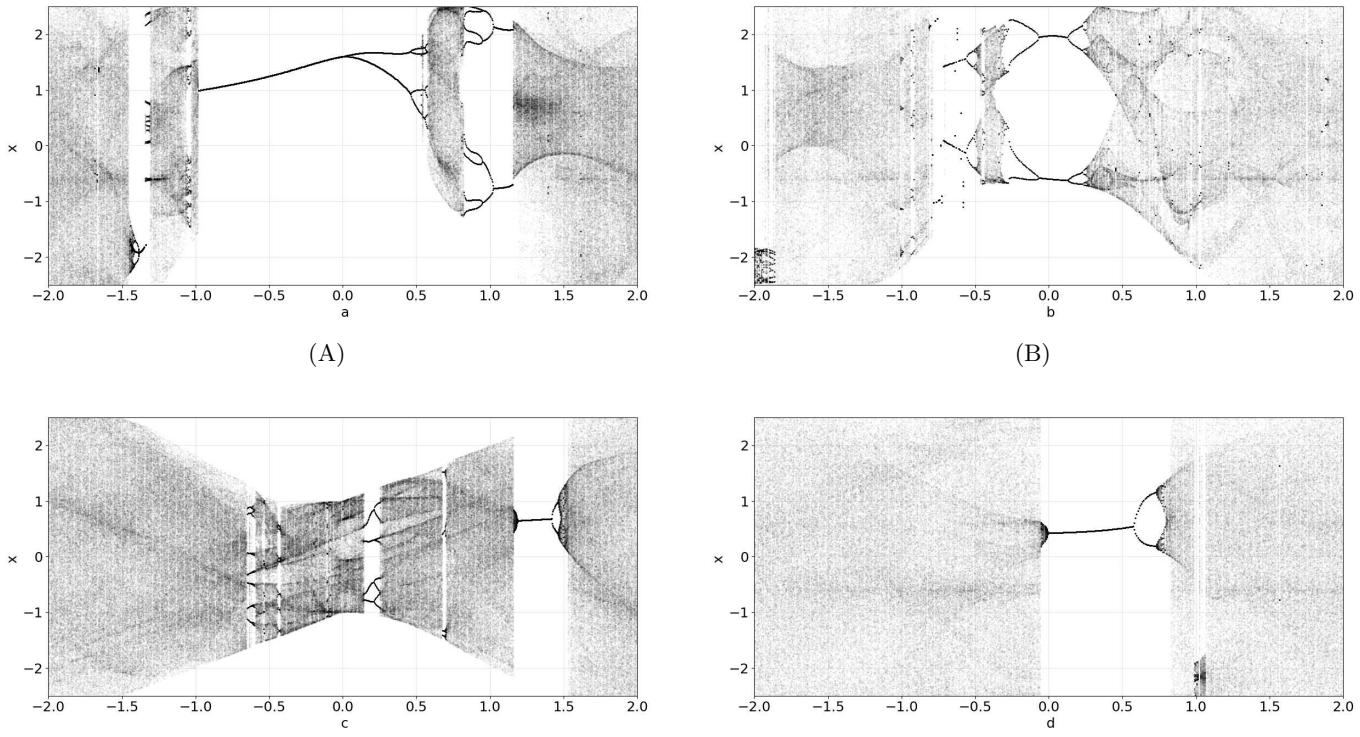


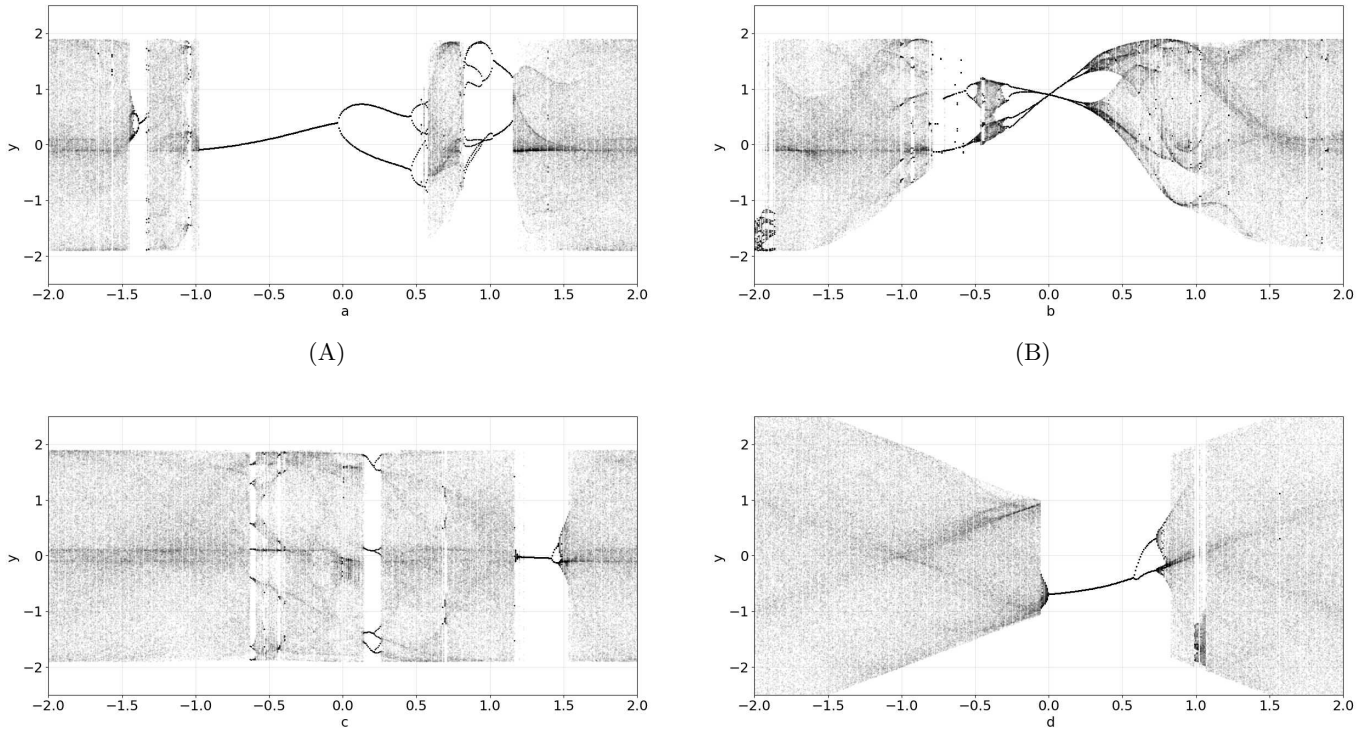
Figure 1: Zoomed bifurcation diagram of the system (1) for parameter c in region $[1.0, 2.0]$, the remaining fixed parameters are $a = 1.5$, $b = -1.8$, and $d = 0.9$. Observe the chaotic regions (dense point clouds), periodic windows (thin bands), period-doubling cascades (progressive branching), and crisis phenomena (sudden vertical expansions).



(A) (B)

(C) (D)

Figure 2: This figure shows bifurcation diagrams of the system (1). The values of x are presented by the vertical axis, while the horizontal axis in each panel corresponds to the parameter being varied. Four parameter sweeps are presented: (A) varying the values of a, and fixed parameters are $b = -1.8, c = 1.6,$ and $d = 0.9$; (B) varying the values of b, and fixed parameters are $a = 1.5, c = 1.6,$ and $d = 0.9$; (C) varying the values of c, and fixed parameters are $a = 1.5, b = -1.8,$ and $d = 0.9$; and (D) varying the values of d, and fixed parameters are $a = 1.5, b = -1.8,$ and $c = 1.6$.



(A) (B)

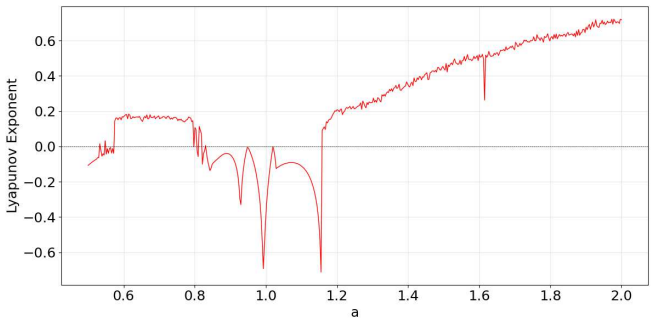
(C) (D)

Figure 3: Bifurcation diagrams of y with respect to parameters. The values of y are represented by the vertical axis, while the horizontal axis in each panel corresponds to the parameter being varied. Four parameter sweeps are presented: (A) varying the values of a, and fixed parameters are $b = -1.8, c = 1.6$ and $d = 0.9$; (B)varying the values of b, and fixed parameters are $a = 1.5, c = 1.6,$ and $d = 0.9$; (C) varying the values of c, and fixed parameters are $a = 1.5, b = -1.8,$ and $d = 0.9$; and (D) varying the values of d, and fixed parameters are $a = 1.5, b = -1.8,$ and $c = 1.6$.

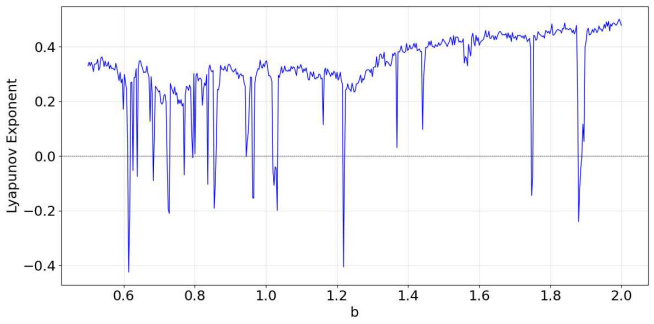
3 Lyapunov Exponents

In this section, we analyze the long-term behavior and topological complexity of the Clifford attractor which are quantitatively characterized by its spectrum of Lyapunov exponents via QR-decomposition [38, 33]. The asymptotic exponential rates of divergence or convergence for infinitesimally close trajectories in the phase space are represented by the Lyapunov exponents.

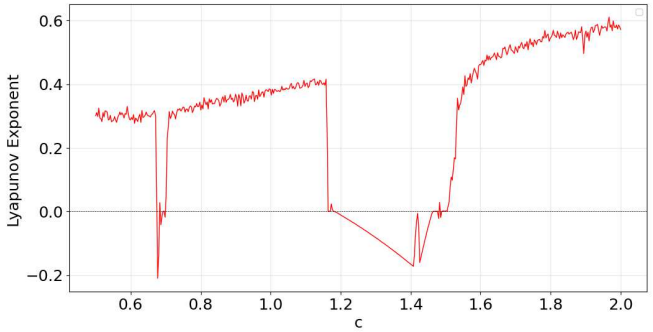
The exponential rate of separation of infinitesimally close trajectories is measured by the Largest Lyapunov Exponent (LLE). The LLE provides a clear diagnostic of the system behavior. A positive value reflects chaos, with trajectories diverging exponentially. A negative value signals stability, as the trajectories converge toward fixed points or periodic motion. When the exponent is exactly zero, the system lies at a bifurcation or follows a neutral orbit, such as a limit cycle in continuous dynamics.



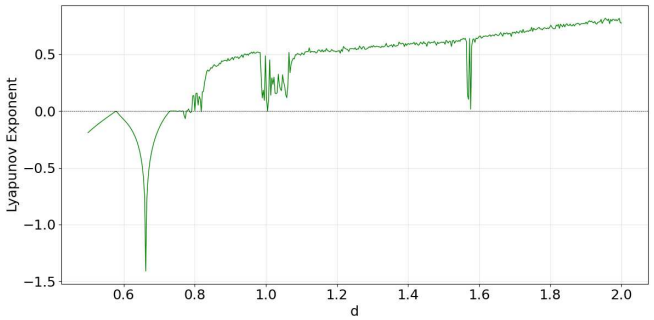
(A) Variation of x with a



(B) Variation of x with b



(C) Variation of x with c



(D) Variation of x with d

Figure 4: Lyapunov exponents of (1) with respect to a, b, c, d. In each panel, the Lyapunov exponent is represented on the vertical axis, while the horizontal axis corresponds to the parameter being varied. The dashed horizontal line at zero marks the critical boundary between stable (negative exponent) and chaotic (positive exponent) dynamics. Four parameter sweeps are shown: (A) variation of d with $a = 1.5, b = -1.8$ and $c = 1.6$; (B) variation of c with $a = 1.5, b = -1.8$ and $d = 0.9$; (C) variation of b with $a = 1.5, c = 1.6$ and $d = 0.9$; and (D) variation of a with $b = -1.8, c = 1.6$ and $d = 0.9$. Regions where the curves lie below zero correspond to stable sinks, while positive values indicate chaotic regimes.

We conduct a full-spectrum Lyapunov analysis for the system (1) while varying a parameter $a \in [0.5, 2.0]$ (with $b = -1.8, c = 1.6, d = 0.9$), which reveals a rich structure (refer to Fig.4(A)). Here we take only the largest eigenvalue λ_1 to quantitatively distinguish between periodic windows and chaotic regimes. In Fig. 4(A), at $a \approx 1.18$, λ_1 crosses zero from below, marking the transition from a stable period-1 orbit to a chaotic attractor. The frequent downward spikes in λ_1 (reaching negative values) identify periodic windows within the chaotic regime. In these windows, λ_1 is negative, indicating that the chaotic attractor has been replaced by a stable periodic orbit. At $a \approx 0.9$ and within the narrow dips (e.g., $a \approx 1.10$), the largest exponent λ_1 is negative, indicating the system settles into a stable fixed point or a periodic orbit. Further, as a increases toward 2.0, λ_1 shows a steady upward trend, indicating increasing levels of complexity and faster divergence rout to chaos.

In Fig. 4(C), the region ($c \approx 1.18$ to $c \approx 1.42$), the LLE λ_1 drops below zero, perfectly matching the single-line region in the bifurcation diagram (refer to Fig. 2(C)). This confirms that the system settles into a stable fixed point ($c = 1.3$ lies deep in this stable negative-LLE trough). In the Chaotic Bands ($c < 1.15$ and $c > 1.55$), the λ_1 is consistently positive ($\approx 0.3 - 0.6$), confirming that the broad clouds in the bifurcation diagram are indeed chaotic (refer to Fig. 2(C)). In the region ($c \approx 1.42$ to $c \approx 1.55$), we see the λ_1 rise from negative values and cross zero at $c \approx 1.42$, which is the exact point where the period-doubling begins in the diagram and oscillates near zero during the doubling sequence before remaining positive as chaos becomes permanent, indicating bifurcation cascades. Further, the sudden drop in λ_1 at $c \approx 1.18$ represents an exterior crisis, where the chaotic attractor is suddenly destroyed and replaced by a stable fixed point. This provides a clear quantitative explanation for the empty region in the bifurcation diagram as in Section 2.

For the other parameters b and d, we can also write the same lines of argument for the LLE that we can see in Fig. 4(B) and 4(D).

4 The 0–1 Test of the System

In this section, we further investigate dynamical transitions within the system (1) using the Gottwald-Melbourne 0–1 test for chaos over the parameter range $c \in [0.5, 2.0]$. This method provides a quantitative approach to distinguish between regular and chaotic dynamics, relying on the time-series output of the system. In contrast to the calculation of Lyapunov exponents, which requires explicit knowledge of the governing difference equations and their Jacobian matrices, the 0–1 test operates directly on a scalar time series of the state variable x. Consequently, it produces a purely statistical binary diagnostic. An asymptotic growth rate of $K \approx 0$ indicates regular dynamics, while $K \approx 1$ signifies the presence of chaos (for details, see [10, 11]).

Algorithmic Framework

Given a scalar time series $\{x_n\}_{n=1}^{N}$ from the Clifford map, we begin with the translational variables

$$p_c(n) = \sum_{j=1}^{n} x_j \cos(jc), \quad q_c(n) = \sum_{j=1}^{n} x_j \sin(jc),$$

where $\{x_j\}$ is the scalar time series and $c \in (0, \pi)$ is fixed.

Let $\mathbb{E}[X]$ denote the expectation of the time series. If x_j has a nonzero mean, then

$$x_j = \mathbb{E}[X] + \tilde{x}_j,$$

where $\tilde{x}_j$ is the zero-mean fluctuation. Substituting $\tilde{x}_j$ into $p_c(n)$ and $q_c(n)$ gives

$$p_c(n) = \mathbb{E}[X] \sum_{j=1}^{n} \cos(jc) + \sum_{j=1}^{n} \tilde{x}_j \cos(jc),$$

$$q_c(n) = \mathbb{E}[X] \sum_{j=1}^{n} \sin(jc) + \sum_{j=1}^{n} \tilde{x}_j \sin(jc).$$

The Mean Square Displacement (MSD) is defined as

$$M_c(n) = \lim_{N\to\infty} \frac{1}{N} \sum_{j=1}^{N} \left[(p_c(j+n) - p_c(j))^2 + (q_c(j+n) - q_c(j))^2 \right].$$

The terms involving $\mathbb{E}[X]$ contribute a deterministic oscillatory part:

$$\Delta p_c^{(\text{mean})}(n) = \mathbb{E}[X] \sum_{j=1}^{n} \cos(jc), \quad \Delta q_c^{(\text{mean})}(n) = \mathbb{E}[X] \sum_{j=1}^{n} \sin(jc).$$

Thus, the squared contribution is

$$\left(\Delta p_c^{(\text{mean})}(n)\right)^2 + \left(\Delta q_c^{(\text{mean})}(n)\right)^2 = \mathbb{E}[X]^2 \left(\left(\sum_{j=1}^{n} \cos(jc) \right)^2 + \left(\sum_{j=1}^{n} \sin(jc) \right)^2 \right).$$

Therefore, the oscillatory contribution due to the mean is

$$\mathbb{E}[X]^2 \cdot \frac{1 - \cos(nc)}{1 - \cos(c)}.$$

Subtracting this term from the raw MSD yields the modified MSD,

$$D_c(n) = M_c(n) - \mathbb{E}[X]^2 \cdot \frac{1 - \cos(nc)}{1 - \cos(c)}.$$

From above, we can ensure that $D_c(n)$ reflects only the diffusive growth of the zero-mean fluctuations $\tilde{x}_j$, removing spurious oscillations caused by the mean.

The final test statistic K is the correlation coefficient between $D_c(n)$ and n for $n = 1, \ldots, n_{max}$.

$$K = \text{corr}(n, D_c).$$

It provides a clear diagnostic of the behavior of the system. $K \approx 1$ reflects the translational variables $\{p_c, q_c\}$ that exhibit Brownian-like motion, signifying chaos. $K \approx 0$ reflects the fact that the variables are bounded, which means regular (periodic or fixed-point) dynamics.

In Fig. 5(C), region $c \in [1.18, 1.48]$, the K-statistic remains near zero, verifying that trajectories in this regime converge to a stable fixed point or periodic cycles. Specifically, at $c = 1.3$, the test unequivocally confirms non-chaotic behavior ($K = 0$). For $c < 1.15$ and $c > 1.55$, the K-statistic attains a value near unity (with minor fluctuations due to numerical noise or small

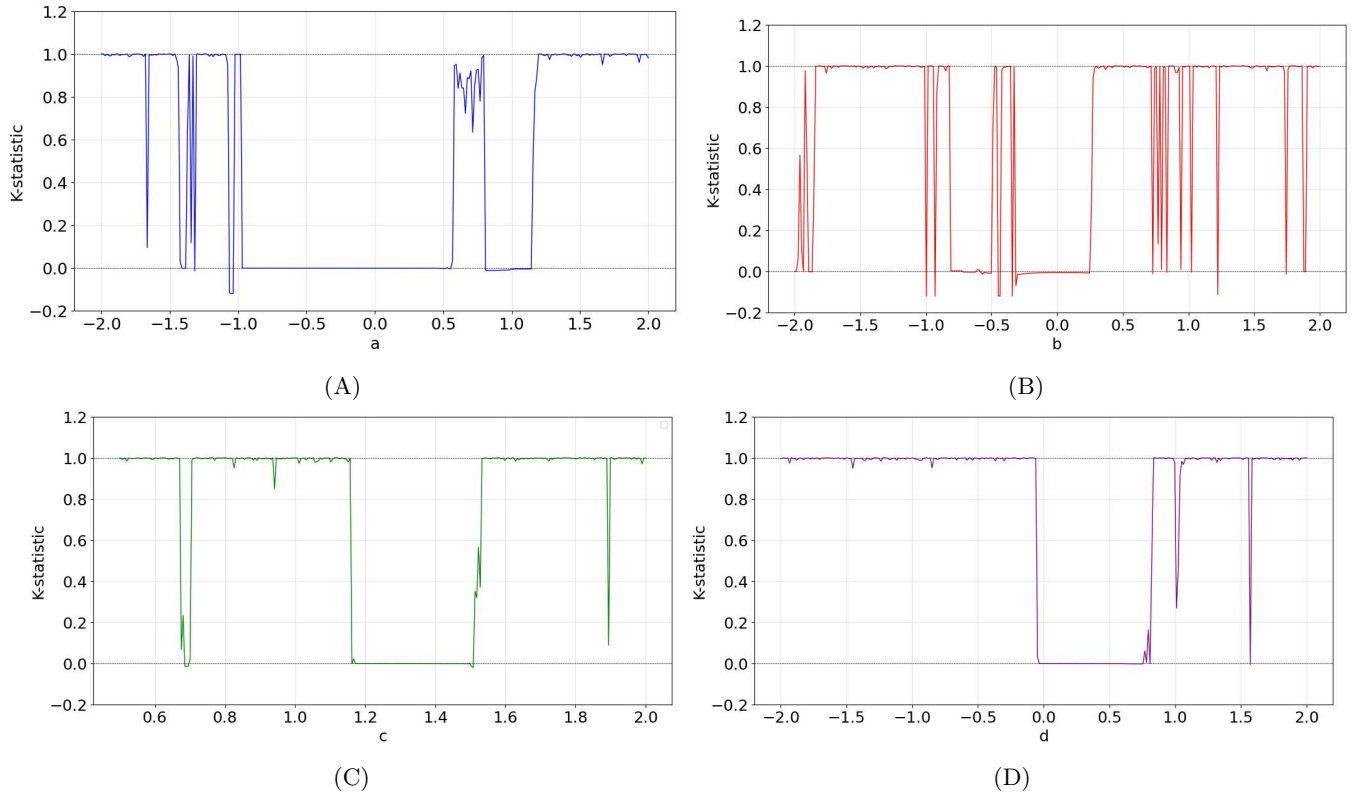


Figure 5: This figure demonstrate quantitative Chaos Characterization via the 0–1 Test. The statistical diagnostic K is plotted on y-axis and the parameters are plotted on x-axis in panel. (A) Variation of parameter a with fix $b = -1.8$, $c = 1.6$, and $d = 0.9$. (B) Variation of parameter b with fix $a = 1.5$, $c = 1.6$, $d = 0.9$. (C) Variation of parameter c with fix $a = 1.5, b = -1.8,$ and $d = 0.9$. (D) Variation of parameter d with fixed $a = 1.5$, $b = -1.8$, $c = 1.6$.

periodic windows). This is a definitive statistical signature of chaos. At $c = 1.5$, the test shows $K \approx 0$, but it immediately jumps toward 1.0 shortly after. This indicates that $c = 1.5$ is likely near a bifurcation point. The sharp drops in K at $c \approx 0.68$ and $c \approx 0.94$ highlight the test's ability to detect narrow periodic windows that may be difficult to resolve in coarse Lyapunov sweeps, as well as the identified periodic windows seen in the previous bifurcation diagram (refer to Section 2). The above observation shows that the 0–1 test acts as an independent validator for the Lyapunov spectrum with more depth confirmation.

We can write the same lines of argument with respect to the other parameters as well (refer to Figs. 5(A), 5(B), and 5(D)). In the upcoming sections, we perform a more detailed analysis, such as fixed point and stability analysis, phase portraits and topological transitions, and basins of attraction.

5 Fixed Point and Their Stability

In accordance with the analytical framework for discrete systems, a fixed point (x^*, y^*) satisfies the equilibrium condition $F(x^*, y^*) = \mathbf{0}$, where the components of the vector field F are defined in Eq. (2) (see for details [23]).

$$\begin{aligned} f_1(x, y) &= \sin(ay) + c\cos(ax) - x, \\ f_2(x, y) &= \sin(bx) + d\cos(by) - y. \end{aligned} \tag{2}$$

The local stability of these equilibrium points is determined by the eigenvalues λ_i of the Jacobian matrix 3 (refer to [26] for details). Following the established criteria for discrete-time stability, a fixed point is locally asymptotically stable if the spectral radius $\rho(J) = \max_i |\lambda_i| < 1$ (see the details [6, 9]).

Define

$$f(x, y) = \sin(ay) + c\cos(ax), \quad g(x, y) = \sin(bx) + d\cos(by).$$

The Jacobian is

$$J(x, y) = \begin{bmatrix} \frac{\partial f}{\partial x} & \frac{\partial f}{\partial y} \\ \frac{\partial g}{\partial x} & \frac{\partial g}{\partial y} \end{bmatrix} = \begin{bmatrix} -ac\sin(ax) & a\cos(ay) \\ b\cos(bx) & -bd\sin(by) \end{bmatrix}. \tag{3}$$

Let (x^*, y^*) be a fixed point of F. The eigenvalues λ of $J(x^*, y^*)$ satisfy $\det(J - \lambda I) = 0$. Explicitly, $\lambda^2 - \mathrm{tr}(J)\lambda + \det(J) = 0$, where $\mathrm{tr}(J) = -ac\sin(ax^*) - bd\sin(by^*)$, $\det(J) = (abcd)\sin(ax^*)\sin(by^*) - ab\cos(ay^*)\cos(bx^*)$.

The fixed point is stable if both eigenvalues satisfy $|\lambda| < 1$ or $\max_i |\lambda_i| < 1$. Equivalently, for a two-dimensional discrete map, stability requires

$$1 + \det(J) + \mathrm{tr}(J) > 0, \quad 1 + \det(J) - \mathrm{tr}(J) > 0, \quad 1 - \det(J) > 0.$$

Example 5.1. *For the parameter set*

$$a = 1.5, \quad b = -1.8, \text{ and } \quad c = 1.3, \quad d = 0.9,$$

the fixed points satisfy

$$x^* = \sin(1.5y^*) + 1.3\cos(1.5x^*), \quad y^* = \sin(-1.8x^*) + 0.9\cos(-1.8y^*).$$

Solving this system numerically gives

$$(x^*, y^*) \approx (0.663, -0.031).$$

The Jacobian is

$$J(x, y) = \begin{bmatrix} -ac\sin(ax) & a\cos(ay) \\ b\cos(bx) & -bd\sin(by) \end{bmatrix}.$$

At the fixed point,

$$J(0.663, -0.031) \approx \begin{bmatrix} -1.635 & 1.498 \\ -0.664 & 0.090 \end{bmatrix}.$$

The eigenvalues of this Jacobian are

$$\lambda_{1,2} \approx -0.772 \pm 0.502i.$$

Their magnitudes are $|\lambda| \approx 0.91$. *Since both eigenvalues satisfy* $|\lambda| < 1$, *the fixed point* $(x^*, y^*) \approx (0.663, -0.031)$ *is stable. This confirms that for* $c = 1.3$, *the Clifford attractor admits a locally attracting fixed point, consistent with bifurcation analysis.*

We analyze the fixed points and their local stability of the system 1, where the fixed parameters are $a = 1.5$, $b = -1.8$, $d = 0.9$, while varying $c \in \{1.2, 1.3, 1.4, 1.5, 1.6\}$, using the initial guess $(0.1, 0.1)$ in a root-finding algorithm that we discussed above, and the summarization is given in Table 2. The Jacobian matrix at each fixed point is computed, and its eigenvalues are used to classify local stability. A fixed point is deemed stable if all eigenvalues lie strictly inside the unit circle ($|\lambda_i| < 1$), and unstable otherwise.

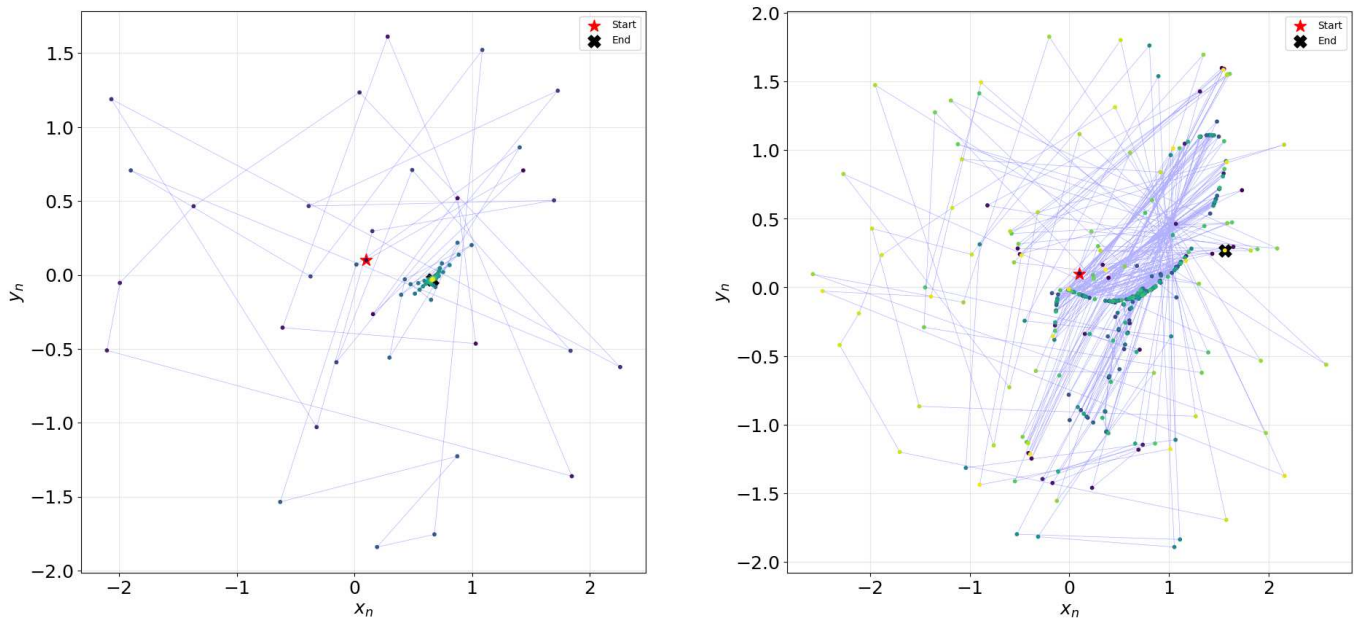
Table 2: Fixed point analysis for selected values of c.

c	Initial Guess	Fixed Point (x^*, y^*)	Eigenvalues $\lambda_{1,2}$	Local Stability
1.2	$(0.1, 0.1)$	$(0.6359, -0.0207)$	$-0.6785 \pm 0.4932i$	**Stable**
1.3	$(0.1, 0.1)$	$(0.6627, -0.0308)$	$-0.7723 \pm 0.5019i$	**Stable**
1.4	$(0.1, 0.1)$	$(0.6769, -0.0405)$	$-0.9621 \pm 0.4826i$	**Stable (borderline)**
1.5	$(0.1, 0.1)$	$(0.6902, -0.0502)$	$-1.3574, -0.4314$	**Unstable**
1.6	$(0.1, 0.1)$	$(0.7030, -0.0599)$	$-1.5127, -0.3982$	**Unstable**

From $c = 1.2$ to $c = 1.3$, the fixed points remain stable, as indicated by complex conjugate eigenvalues that are less than unity. In Table 2, at $c = 1.4$, the eigenvalues reach approximately unity, which causes the appearance of instability. Also, at $c = 1.5$ and $c = 1.6$, one eigenvalue at both points is larger in magnitude than the value 1, making the fixed point unstable (this will also be seen and confirmed in Section 6 via phase portrait). This kind of transition is known for the period-doubling cascade, which then routes to chaos. This can also be observed in the iterative phase plane path (phase-plane cobweb) in Fig. 6. We can see that for the stable regime ($c = 1.3$), the iterative path forms a complex spiral that converges to the primary fixed point. In contrast, in the chaotic regime ($c = 1.6$), the iterative path diverges.

6 Phase Portrait and Topological Transition

Visual dynamical transitions are presented in this section by comparing their phase portraits at different values of the parameter.



(A) Iterative path for ($c = 1.3$)

(B) Iterative path for ($c = 1.6$)

Figure 6: This figure illustrates the phase-plane trajectories of the system (1) at $c = 1.3$ and $c = 1.6$ and other fixed parameters are $a = 1.5, \quad b = -1.8, \quad d = 0.9$. Each orbit start at the red star and end at the black cross. The blue curve traces the iterative path, the scatter points are colored by iteration index using the viridis colormap (purple → blue → green → yellow). The gradient indicates time progression where darker shades mark earlier steps, brighter tones mark later ones. By this way it is showing how the orbit evolves toward its final state in each panel. In Left panel (A), at $c = 1.3$, the iterative path forms a complex spiral converging to the primary fixed point where as in right panel (B) at $c = 1.6$ produces an aperiodic web that fills the invariant set of the strange attractor.

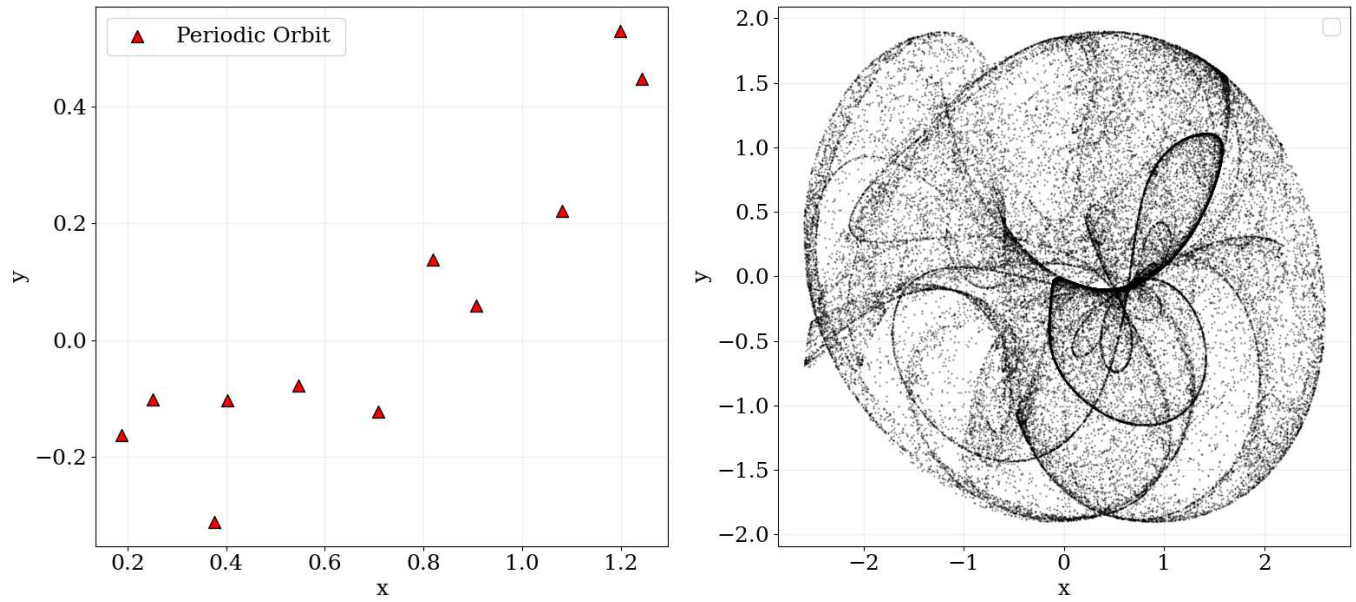


Figure 7: This figure depicts the transition from periodic motion to chaos in the system (1). On the left, the phase portrait at $c = 1.5$ with $a = 1.5, \quad b = -1.8, \quad d = 0.9$ settles into a stable period-11 orbit, marked by red triangles. This illustrates the high-order regular dynamics near the bifurcation threshold. On the right, the portrait at $c = 1.6$ (remaining the same parameters) reveals a strange attractor, plotted as black dots. The attractor highlights the space-filling complexity and fractal geometry characteristic of fully developed chaos.

At $c = 1.5$, in the left Fig. 7, we can observe that the global dynamics settle onto a stable Period-11 orbit, indicating that the primary fixed point is a saddle point. The attractor's periodically visited states are represented by the eleven discrete points (red triangles). This state represents the pre-chaotic phase of the system (1), where the complexity is high, but the motion remains deterministic and periodic, resulting in a zero growth rate ($K \approx 0$ in the 0–1 test), as stated in Section 4.
In right Fig. 7, increasing the parameter to $c = 1.6$ triggers the final transition to the chaotic regime. The resulting strange attractor exhibits the hallmark properties of deterministic chaos.

7 Basin of Attraction

In this section, we explore the global stability of the system (1) by examining its basins of attraction in different dynamical regimes. Formally, the basin of attraction $\mathcal{B}(\mathcal{A})$ is the collection of initial conditions $\mathbf{x}_0 \in \mathbb{R}^2$ for which the trajectory $\phi^n(\mathbf{x}_0)$ converges to the invariant set $\mathcal{A}$ as $n \to \infty$ as shown in [34]. The collection is

$$\mathcal{B}(\mathcal{A}) = \{\mathbf{x}_0 \in \mathbb{R}^2 : \lim_{n\to\infty} \text{dist}(\phi^n(\mathbf{x}_0), \mathcal{A}) = 0\}.$$

Visualization and Analysis

We generate convergence maps for the system (1) at parameter values $c = 1.3$ and $c = 1.5$ with $a = 1.5, \quad b = -1.8, \quad d = 0.9$ to study global stability and the associated basin structure. The basin of attraction, $\mathcal{B}(\mathcal{A})$, consists of all initial conditions (x_0, y_0) whose trajectories asymptotically converge to the invariant set $\mathcal{A}$.

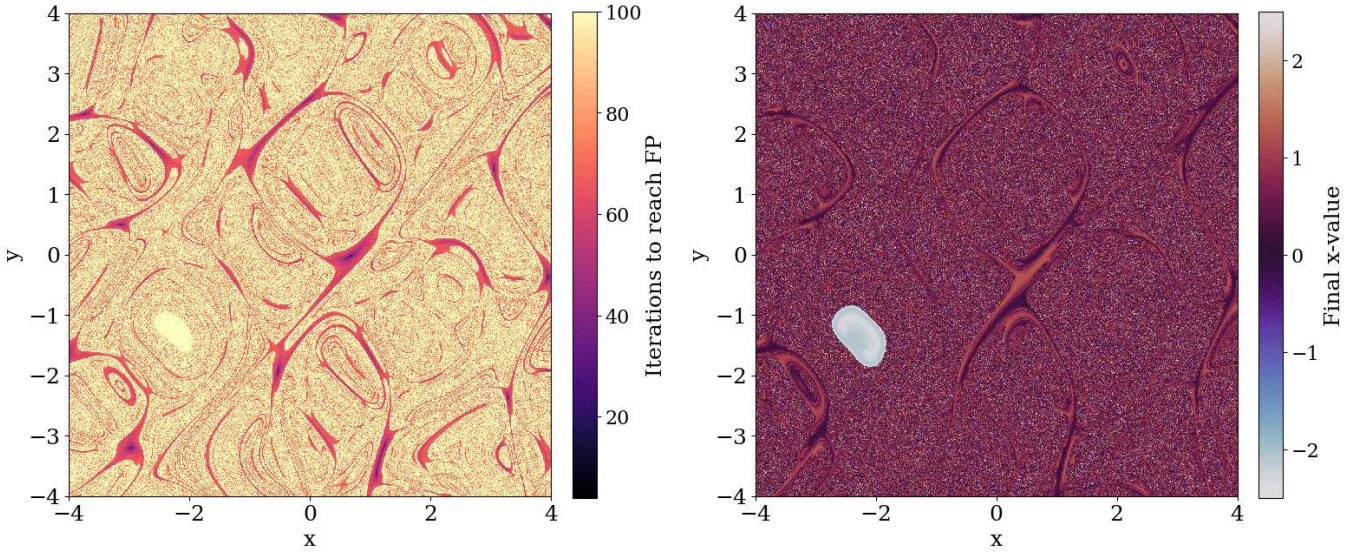


Figure 8: Global Stability and Basin Structure Transitions. A comparative analysis of the Clifford attractor's response to initial conditions across the $[-4, 4] \times [-4, 4]$ phase plane. (a) Left panel (at $c = 1.3$ with $a = 1.5, \quad b = -1.8, \quad d = 0.9$) shows mapping of convergence speed to the stable fixed point, where smooth ripples indicate the manifold structure (colorbar: iterations to converge). (b) Right panel (at $c = 1.5$ with $a = 1.5, \quad b = -1.8, \quad d = 0.9$) displays the final x coordinate after iteration for each initial condition (colorbar: final x value), revealing final-state sensitivity, fractal-like topography and mixing properties characteristic of a strange attractor with a positive Lyapunov exponent. Axes are labeled in phase variables, the horizontal axis is x and the vertical axis is y.

In Fig. 8, we visualize the basins of attraction for $c = 1.3$ and $c = 1.5$ on a grid of the phase plane $[-4, 4] \times [-4, 4]$. At $c = 1.3$ (left in Fig. 8), the dynamics show a stable spiral sink that indicates the convergence map. The basin appears smooth, which means that, at most initial conditions in the range $[-4, 4]$, solutions converge rapidly to the fixed point $(0.6627, -0.0308)$ (see Section 5). Within the domain $[-4, 4] \times [-4, 4]$, there are no divergent regions, indicating that this fixed point acts as a global attractor (this will also be confirmed in Section 8). The rippled structures indicate the isochronic contours, and they also indicate the spiraling manifolds, which actually reveal that the Jacobian (3) has complex eigenvalues. Dark central regions mark points that settle quickly, while lighter bands represent trajectories that undergo additional rotations before convergence. We can observe that escape boundaries are not present in this range, which confirms that the particular point is the globally attractive fixed point. Because of the trigonometric periodicities, there is symmetry in convergence.

At $c = 1.5$ (right in Fig. 8), due to the instability of the fixed point, we can observe that the smooth basin transforms into a highly mixed set. The convergence map shows an intricate, non-smooth structure that evolves into a fractal-like form, which indicates a slightly high-entropy pattern (we will see in Section 11). Observe that curvilinear ghost structures are visible in the map, indicating unstable manifolds of the chaotic set; it also shows a kind of stretching and folding mechanism that drives the positive Lyapunov exponent (as shown in Section 3). Despite this extreme sensitivity, the colors remain bounded, confirming that the system can be dissipative (we will see Section 9).

8 Sensitivity to Initial Conditions

In this section, we investigate sensitivity with respect to the initial conditions. Sensitivity to initial conditions (SIC) is the definitive hallmark of deterministic chaos. It implies that for any given initial state $\mathbf{u}_0$, a perturbed state $\mathbf{u}_0 + \delta_0$ will deviate from the original trajectory at an exponential rate, rendering long-term prediction impossible despite the deterministic nature of the governing equations [25]. We perform a high-precision simulation using an infinitesimal initial separation of $\delta_0 = 10^{-10}$ to quantify this phenomenon in the system (1).

Given an initial condition $u_0 = (x_0, y_0)$, the trajectory evolves as $u_n = F^n(u_0)$. Consider an initial perturbation condition $fu_0' = u_0 + \boldsymbol{\delta}_0$, with $\boldsymbol{\delta}_0 = (\delta_x, \delta_y)$ small. The perturbed trajectory evolves as $u_n' = F^n(u_0')$. The instantaneous separation

vector is

$$\boldsymbol{\delta}(n) = u'_n - u_n = \big(x'_n - x_n,\ y'_n - y_n\big).$$

The Euclidean distance between the two trajectories is

$$\delta(n) = \|\boldsymbol{\delta}(n)\| = \sqrt{(x'_n - x_n)^2 + (y'_n - y_n)^2}.$$

In a chaotic regime, the separation grows approximately exponentially:

$$\delta(n) \approx \delta(0)e^{\lambda_1 n},$$

where λ_1 is the LLE. Taking logarithms yields

$$\ln \delta(n) \approx \ln \delta(0) + \lambda_1 n.$$

Thus, plotting $\ln \delta(n)$ against n produces a straight line whose slope provides a direct time-domain estimate of the LLE. This method corresponds exactly to the numerical procedure implemented in our simulations. Two trajectories are evolved under the system (1), their Euclidean separation $\delta(n)$ is recorded, and the slope of $\ln \delta(n)$ in the linear regime is used to estimate λ_1.

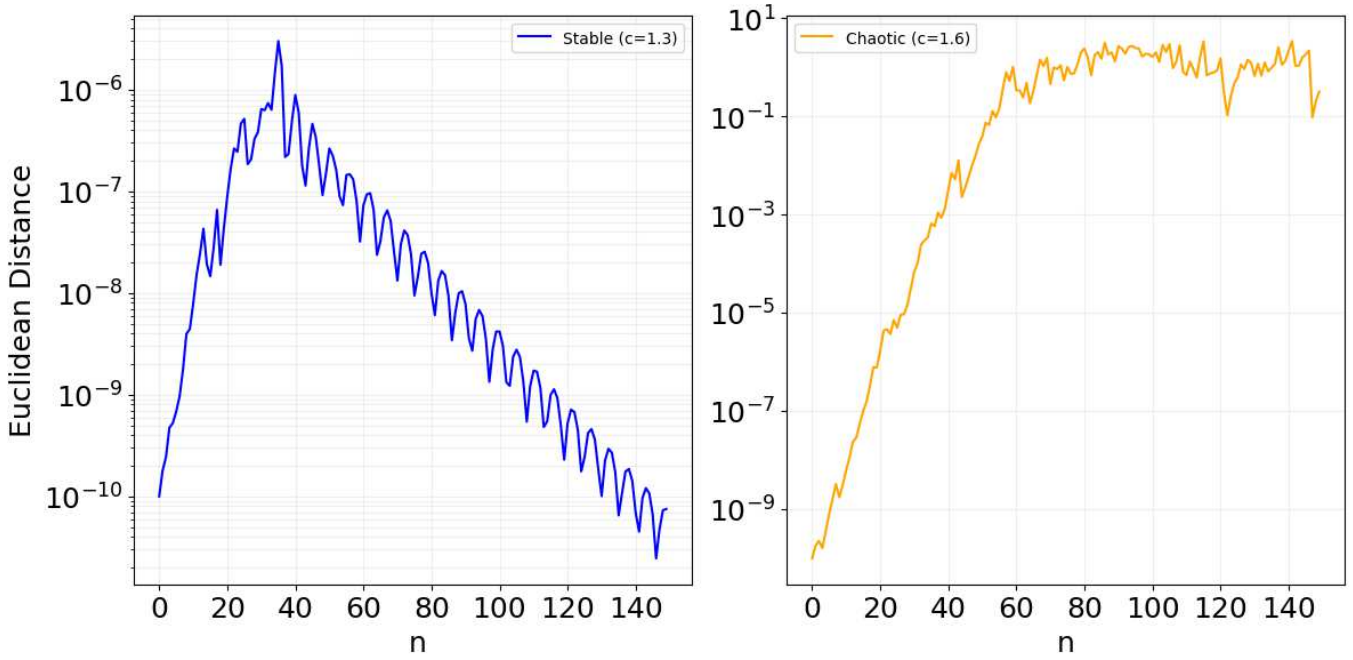


Figure 9: Evolution of Trajectory Separation in Stable vs. Chaotic Regimes. Plot is $\ln \delta(n)$ (logarithmic value of Euclidean distance) against n. Left panel, in the stable regime (at $c = 1.3$ with $a = 1.5,\quad b = -1.8,\quad d = 0.9$), the initial perturbation decays exponentially after a brief transient, signifying a self-correcting system. Right panel, in the chaotic regime (at $c = 1.6$ with $a = 1.5,\quad b = -1.8,\quad d = 0.9$), the separation grows linearly in log-space (exponentially in linear space), matching the theoretical LLE (Section 3). Saturation occurs at $n \approx 70$, representing the total loss of predictability.

In the left panel of Fig. 9, in $c = 1.3$ with fixed parameters $a = 1.5, b = -1.8$, and $d = 0.9$, the initial point $(x_0, y_0) = (0.1, 0.1)$ illustrates the separation distance $\delta(n)$, showing a downward trend after an initial transient phase. This self-correcting behavior confirms that the fixed point $(x^*, y^*) = (0.6627, -0.0308)$ acts as a global sink; any infinitesimal perturbation is exponentially suppressed, confirming the system's robustness to initial-condition errors and small perturbations are forgotten, making the system predictable.

In the right panel of Fig. 9, in $c = 1.6$ with fixed parameters $a = 1.5, b = -1.8$, and $d = 0.9$, and the initial point is $(x_0, y_0) = (0.1, 0.1)$) illustrates a robust linear increase in $\ln \delta(n)$ for $n \in [0, 60]$. The calculated slope of ≈ 0.408 is in excellent agreement with our previously derived LLE of $\lambda_1 \approx 0.42$. Thus, it confirms that the trajectories diverge by a factor of $e^{0.41} \approx 1.5$ per iteration. At approximately $n \approx 70$, the divergence ceases to be exponential and fluctuates around a constant value of ≈ 1.0. This saturation marks the point at which the two trajectories have become completely uncorrelated.

Here, we have done only for two values of c, but we can perform a similar analysis to $c \in [-2.0, 2.0]$ and write a demonstration based on the same lines. Not only for c and x, this can be done with respect to any parameters a, b and d, and the variable y.

In the upcoming sections, we have analyzed the geometric complexity and fractal structure through fractal dimension and correlation dimension

9 Fractal Dimension and the Kaplan–Yorke Conjecture

In this section, we analyze the geometric complexity. The geometric complexity and information-processing capacity of a chaotic attractor are quantified by its fractal dimension D. For the system (1), we employ the Kaplan–Yorke dimension (D_{KY}),

also known as the Lyapunov dimension. This diagnostic connects the topological structure of the attractor to its fundamental dynamical rates, the Lyapunov spectrum $\{\lambda_1, \lambda_2\}$ [18, 38]. For a two-dimensional discrete-time map with ordered Lyapunov exponents $\lambda_1 \geq \lambda_2$, the Kaplan–Yorke conjecture specifies the dimension as

$$D_{KY} = \begin{cases} 1 + \dfrac{\lambda_1}{|\lambda_2|}, & \text{if } \lambda_1 \geq 0 \text{ and } \lambda_1 + \lambda_2 < 0, \\ 2, & \text{if } \lambda_1 + \lambda_2 \geq 0, \\ 0, & \text{if } \lambda_1 < 0. \end{cases}$$

The first case corresponds to dissipative chaos with a fractional dimension between 1 and 2. The second case arises when the sum of exponents is non-negative, in which case the attractor saturates the embedding dimension. The third case indicates global stability with no chaotic dynamics. Thus, D_{KY} provides a continuous measure interpolating between a one-dimensional curve ($D = 1$) and a two-dimensional space-filling set ($D = 2$), with fractional values quantifying the scaling complexity of the attractor's transverse structure (see for details [26]).

Dissipative (Thin) vs. Non-Dissipative (Fat) Topology

Unlike many standard chaotic systems, the system is not strictly dissipative. Depending on the parameters (a, b, c, d), it may exhibit either global area contraction or expansion, giving rise to distinct geometric archetypes.

Dissipative (Thin) Fractal

In Fig. 10 (left panel), parameters $a = 1.6, b = -0.6, c = -1.2,$ and $d = 1.6$, the Lyapunov spectrum is

- $\lambda_1 \approx 0.1681$,
- $\lambda_2 \approx -0.5838$,
- $\sum \lambda_i \approx -0.4157$.

The Kaplan–Yorke formula gives

$$D_{KY} = 1 + \frac{0.1681}{|-0.5838|} \approx 1.2879.$$

The fractal components are quantified by the thickness of the fractal layers. This dimension indicates a thin fractal set, a Cantor-like structure that is geometrically more complex than a one-dimensional curve yet still occupies zero measure in the two-dimensional plane.

Non-Dissipative Chaotic Attractor

In Fig. 10 (right panel), parameters $a = 1.5, b = -1.8, c = 1.6,$ and $d = 0.9$, the Lyapunov spectrum is

- $\lambda_1 \approx 0.4555$,
- $\lambda_2 \approx -0.1704$,
- $\sum \lambda_i \approx 0.2851$.

In this case, from the Kaplan–Yorke formula, unlike its usual dissipative form, the attractor saturates the embedding dimension

$$D_{KY} = 2.0.$$

This implies that the system remains chaotic ($\lambda_1 > 0$), its invariant measure fills the two-dimensional phase space. The strong folding induced by the trigonometric terms produces a non-dissipative chaotic attractor with full two-dimensional support, which is sometimes informally described as a fat attractor. Unlike Cantor-like fractals of fractional dimension, this attractor possesses maximal capacity and does not exhibit voids or gaps in the plane.

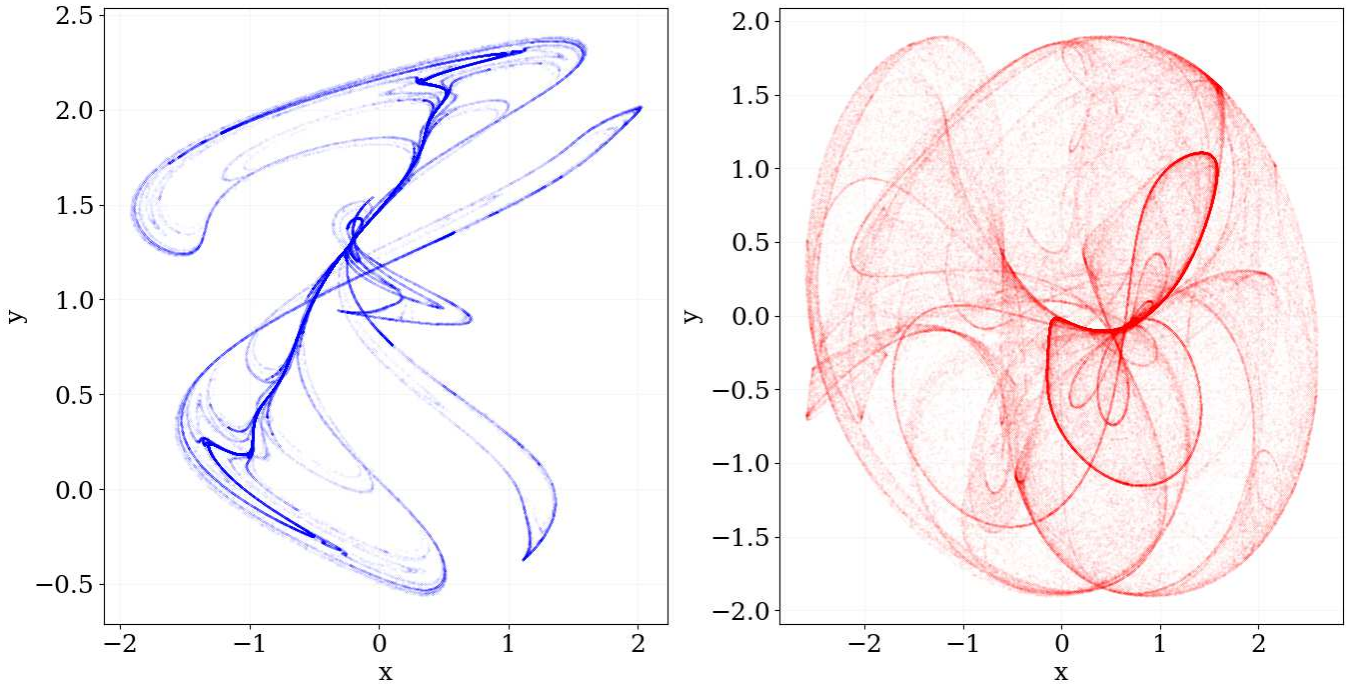


Figure 10: This figure shows the comparison of fractal geometries in the system (1). The left panel displays the dissipative, thin-fractal attractor generated with parameters $a = 1.6$, $b = -0.6$, $c = -1.2$, and $d = 1.6$; the right panel shows the non-dissipative, fat attractor with $a = 1.5$, $b = -1.8$, $c = 1.6$, and $d = 0.9$.

10 Correlation Dimension and Grassberger-Procaccia Analysis

In this section, we find an alternative method to measure the fractal structure of the attractor and focus mainly on the density of pairs of points in the phase space through the correlation dimension D_2. To further characterize the attractor's complexity, we perform a Grassberger-Procaccia analysis to estimate the Correlation Dimension (D_2). This is a measure of the scaling behavior of the points' spatial distribution and represents a lower bound on the information dimension [12].

Definition 10.1. *The correlation integral $C(r)$ is defined as the fraction of pairs of points in the data set whose Euclidean distance is less than r:*

$$C(r) = \lim_{N\to\infty} \frac{2}{N(N-1)} \sum_{i=1}^{N} \sum_{j=i+1}^{N} \Theta(r - \|\mathbf{x}_i - \mathbf{x}_j\|),$$

where Θ is the Heaviside step function.

It is known that for a fractal set, $C(r)$ scales as a power law for small r; that is, $C(r) \sim r^{D_2}$.

Definition 10.2. *[13] The correlation dimension D_2 is thus extracted as the slope of the linear region in a log-log plot*

$$D_2 = \lim_{r\to 0} \frac{\ln C(r)}{\ln r}.$$

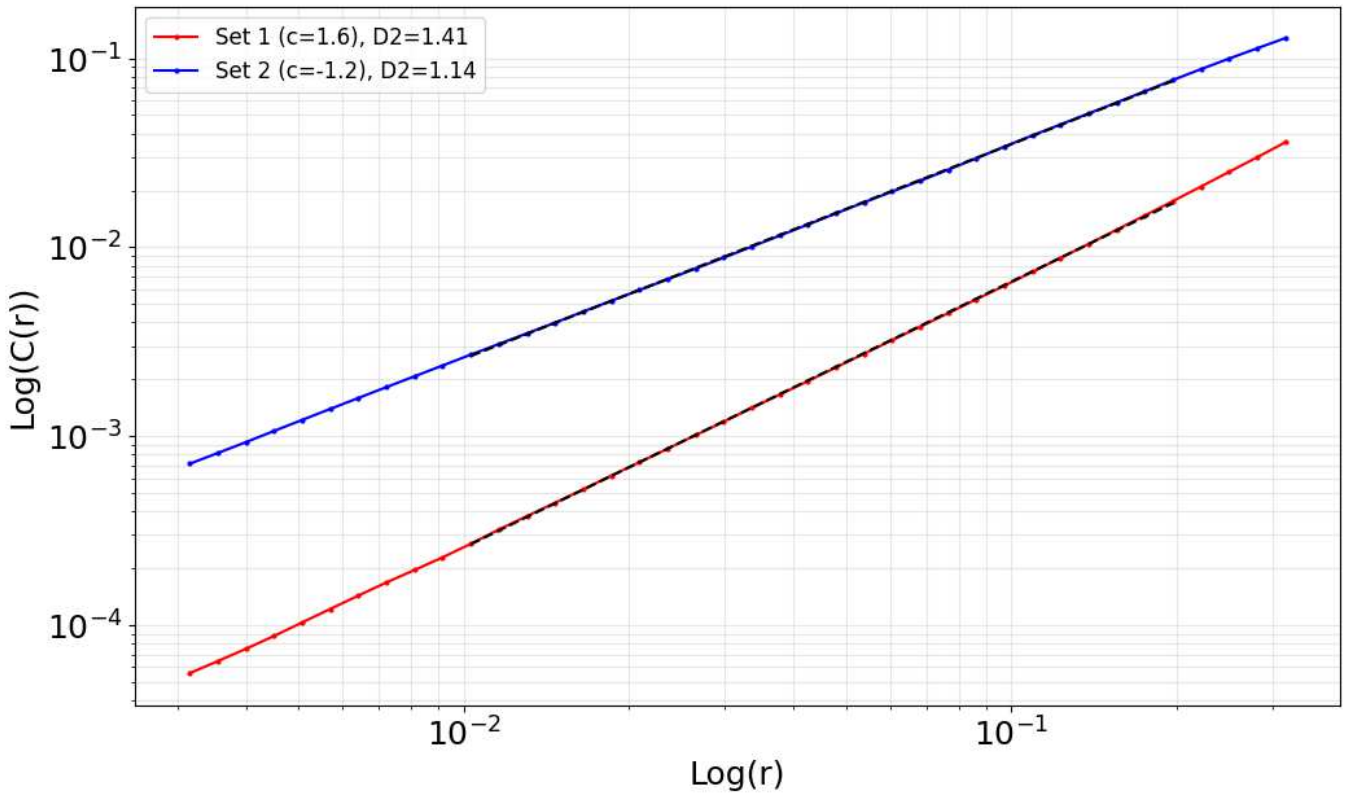


Figure 11: Correlation Integral and Scaling Analysis. The log-log plot of $C(r)$ vs. r illustrates the power-law scaling for $c = 1.6$ (with fixed parameters $a = 1.5,\ b = -1.8,\ $ and $d = 0.9$) and $c = -1.2$ (with fixed parameters $a = 1.6, b = -0.6,\ $ and $d = 1.6$).

At $c = 1.6$ (with fixed parameters $a = 1.5,\ b = -1.8,\ $ and $d = 0.9$), we estimate $D_2 \approx 1.41$ (using the Python code). Observe that $D_2 < D_{KY} = 2.0$ (as D_{KY} is discussed in Section 9); this inequality indicates a difference between the geometric capacity (where the attractor eventually fills the plane) and the actual correlation structure. The correlation dimension D_2 is sensitive to the multifractal distribution of the points. The result 1.41 suggests that although the system as a whole expands areas, the points still cluster along the dominant filamentary structures.

For the fractal regime at $c = -1.2$ (with fixed parameters $a = 1.6, b = -0.6,\ $ and $d = 1.6$), we estimate $D_2 \approx 1.14$ (using the Python code). This is fairly close to $D_{KY} \approx 1.29$ (D_{KY} is discussed in Section 9), which is typical of a thin strange attractor whose points remain tightly confined to a fractal set. In this case, the inequality $D_2 \leq D_{KY}$ is satisfied, (consistent with the expected behavior of attractors). In Fig. 11, the linear fit in the identified scaling region $10^{-2.2} < r < 10^{-1}$ provides a precise estimate of the correlation dimension, confirming the topological shift from thin fractals to non-uniform space-filling sets.

11 Entropy

In this section, through the seven entropy measures, we have analyzed the complete complexity profile on the parameter $c \in [0.5, 2.0]$ (with fixed parameters $a = 1.5, b = -1.8,\ $ and $d = 0.9$) of the system (1). Each type of entropy measures the different dynamical behaviors of the system. Entropies like Kolmogorov-Sinai (KS) entropy quantify information production rates and connect directly to exponential orbit divergence via Pesin's formula [27]. Permutation entropy provides a robust ordinal-pattern-based complexity measure resistant to observational noise [2], and Shannon entropy characterizes the statistical distribution of trajectories in phase space [32]. Similarly, other entropies are present. The combination of the study of multi-faceted entropy with a bifurcation diagram reveals an intricate relationship between parameter values and regimes. For parameter value c, we have generated trajectories by taking the initial condition $(x_0, y_0) = (0.1, 0.1)$, with 300 iterations discarded to ensure convergence to the attractor, 2000 iterations retained for entropy calculations, and the sampling resolution set to 100 equally-spaced values of c across the parameter range.

Kolmogorov-Sinai Entropy

The average rate of information production is quantified by the Kolmogorov-Sinai (metric) entropy. For this discrete-time system, we estimate it via the LLE λ_1,

$$h_{KS} \approx \max(0, \lambda_1),$$

where λ_1 is computed using the Jacobian matrix method [27, 20] (also, we can see in Section 3).

Shannon, Rényi, and Tsallis Entropies

The uncertainty in the spatial distribution of the trajectory is quantified by these entropies. Shannon entropy H_S is the standard measure [32], while Rényi (H_α) and Tsallis (H_q) entropies generalize it by weighting the state probabilities differently[31, 35].

Permutation, Approximate, and Sample Entropies

The permutation entropy (h_p) quantifies the complexity based on ordinal patterns [2]. The approximation entropy (ApEn) and sample entropy (SampEn) measure the regularity and predictability of the sequence, with SampEn being more robust as it eliminates self-matches [29, 30].

Results

The individual evolution of each entropy metric is depicted in Fig. 12. With the variation of c, each subfigure in Fig. 12 reveals a unique signature complexity of the Clifford attractor.

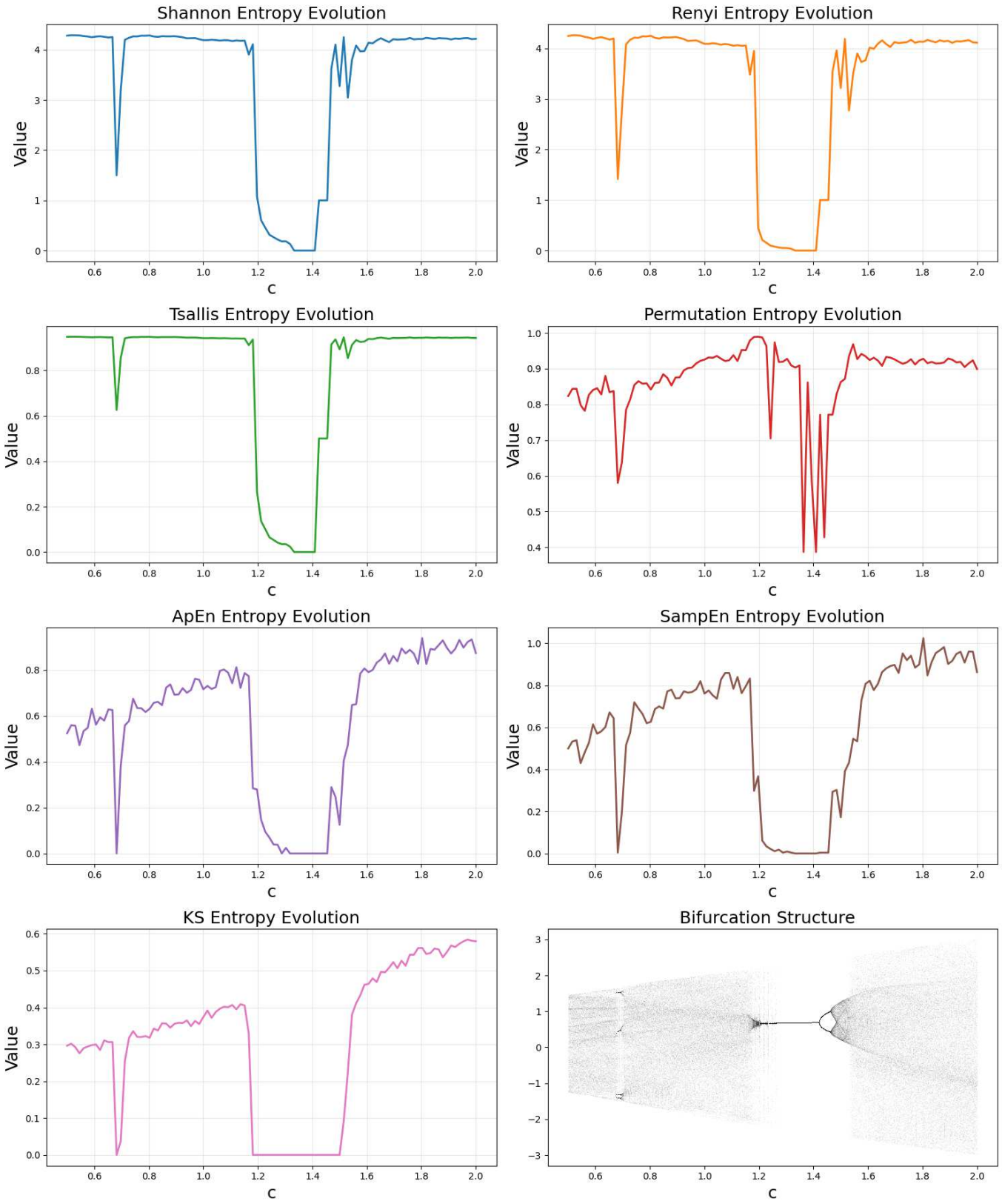


Figure 12: This figure presents individual entropy profiles as $c \in [0.5, 2.0]$ with fixed parameters $a = 1.5$ and $b = -1.8$, and $d = 0.9$. It displays the evolution of Kolmogorov–Sinai entropy (h_{KS}), Shannon entropy (H_S), Rényi entropy (H_α), Tsallis entropy (H_q), permutation entropy (h_p), approximate entropy (ApEn), and sample entropy (SampEn). A grey-scale bifurcation diagram of the attractor is shown in the background to provide direct visual context between entropy variations and changes in dynamical regime.

Table 3: Summary statistics across $c \in [0.5, 2.0]$.

Entropy Measure	Mean	Std. Dev.	Min	Max
KS Entropy (h_{KS})	0.3122	0.1994	0.0000	0.5842
Shannon Entropy (H_S)	3.4521	1.5038	0.0000	4.2919
Rényi Entropy (H_α)	3.3490	1.5194	0.0000	4.2627
Tsallis Entropy (H_q)	0.7893	0.3238	0.0000	0.9479
Permutation Entropy (h_p)	0.8709	0.1106	0.3869	0.9896
Approximate Entropy (ApEn)	0.5813	0.3085	0.0000	0.9390
Sample Entropy (SampEn)	0.5945	0.3274	0.0000	1.0246

Shannon, Rényi, and Tsallis Entropies In Fig. 12, these three entropies exhibit nearly identical trajectories, characterized by a rapid rise followed by a high-entropy plateau. Sharp drops at specific c values, (for example, $c \approx 0.7$ and $c \approx 1.25$) indicate periodic windows where the attractor collapses into a low-dimensional manifold, significantly reducing spatial uncertainty.

Kolmogorov-Sinai (KS) Entropy In the Shannon Entropy Evolution sub-Fig. 12, the path trajectory tracks the chaoticity of the system. From Table 3, the mean is 0.3122, the maximum is 0.5842, and the positive values throughout most of the range confirm that there is deterministic chaos in most of the parameter range. As the peak is near $c \approx 2.0$, we can confirm that information production is maximized at higher scaling factors.

Permutation Entropy From Table 3, a mean of 0.8709, a maximum of 0.9896, and it reaches its maximum ($h_p \approx 0.99$) (refer to the Permutation Entropy Evolution sub-Fig. 12), permutation entropy shows that nearly all possible ordinal patterns are explored in chaotic regions. The clear dip around $c \approx 1.4$ (also visible in Table 3, min = 0.3869) matches the periodic window seen in the bifurcation diagram.

ApEn and SampEn In the ApEn Entropy Evolution and SampEn Entropy Evaluation sub-Fig. 12, the Approximate entropy and the Sample entropy show the most granular sensitivity. The flat-line zeros in these plots (particularly for $c \in [1.2, 1.4]$) represent regions of extreme regularity. The jagged peaks in chaotic regimes highlight the sensitive nature of these algorithmic measures to subtle changes in the attractor's structural density.

Entropies Correlation with Bifurcation

In Fig. 12 and Table 3, we see that for c in $[0.5, 1.1]$ and again in $[1.6, 2.0]$, all entropies reach high values. These are exactly the ranges of the parameter c where the bifurcation diagram shows a dense cloud. The KS entropy stays above 0.7; it shows that the Lyapunov exponents are positive (see Section 3). The permutation entropy also gets closer to its maximum, $h_p > 0.85$, shows the characteristic of a high ordinal pattern and indicates the diversity of chaotic attractors (we can see this in Section 6). Shannon entropy, too, is elevated ($H_S > 3.0$), indicating a broad spatial distribution throughout the phase space (we can see this in Section 12). The positive KS entropy satisfies the mathematical definition of deterministic chaos, and the high permutation entropy distinguishes these regions from stochastic noise.

In Fig. 12, at $c \approx 1.3$ in region $[1.2, 1.4]$, the bifurcation diagram shows clear horizontal bands, which are periodic orbits, and it is also observed in the entropies that there are large drops in Fig 12. KS entropy drops almost to zero (which makes sense because periodic orbits have zero Lyapunov exponents 3). The permutation entropy also decreases, $h_p < 0.6$, reflecting reduced pattern diversity in periodic dynamics. Shannon entropy hits pronounced minima, sometimes near zero, because the trajectory gets stuck on a low-dimensional periodic orbit.

In region $c \in [1.6, 2.0]$, all seven entropy measures fluctuate fast (see Figs. 12 and 13), with sharp ups and downs over small parameter changes in c. Those rapid oscillations in the entropy curves suggest that there are periodic windows in between the chaos

In Fig. 13, the normalized comparison panel also reveals strong qualitative agreement among all seven entropy measures. All entropy types simultaneously reach maxima in chaotic regions and minima in periodic windows, providing cross-validation of dynamical regime identification.

Table 4: Dynamical regime classification based on entropy signatures.

Regime	KS Entropy	Perm. Entropy	Shannon Entropy
Strongly Chaotic	$h_{KS} > 0.8$	$h_p > 0.9$	$H_S > 3.5$
Weakly Chaotic	$0.6 < h_{KS} < 0.8$	$0.7 < h_p < 0.9$	$2.0 < H_S < 3.5$
Transitional	$0.3 < h_{KS} < 0.6$	$0.5 < h_p < 0.7$	$1.0 < H_S < 2.0$
Periodic	$h_{KS} < 0.3$	$h_p < 0.5$	$H_S < 1.0$

This classification scheme, validated by cross-referencing with bifurcation diagram structures, enables systematic identification of dynamical behavior across parameter space.

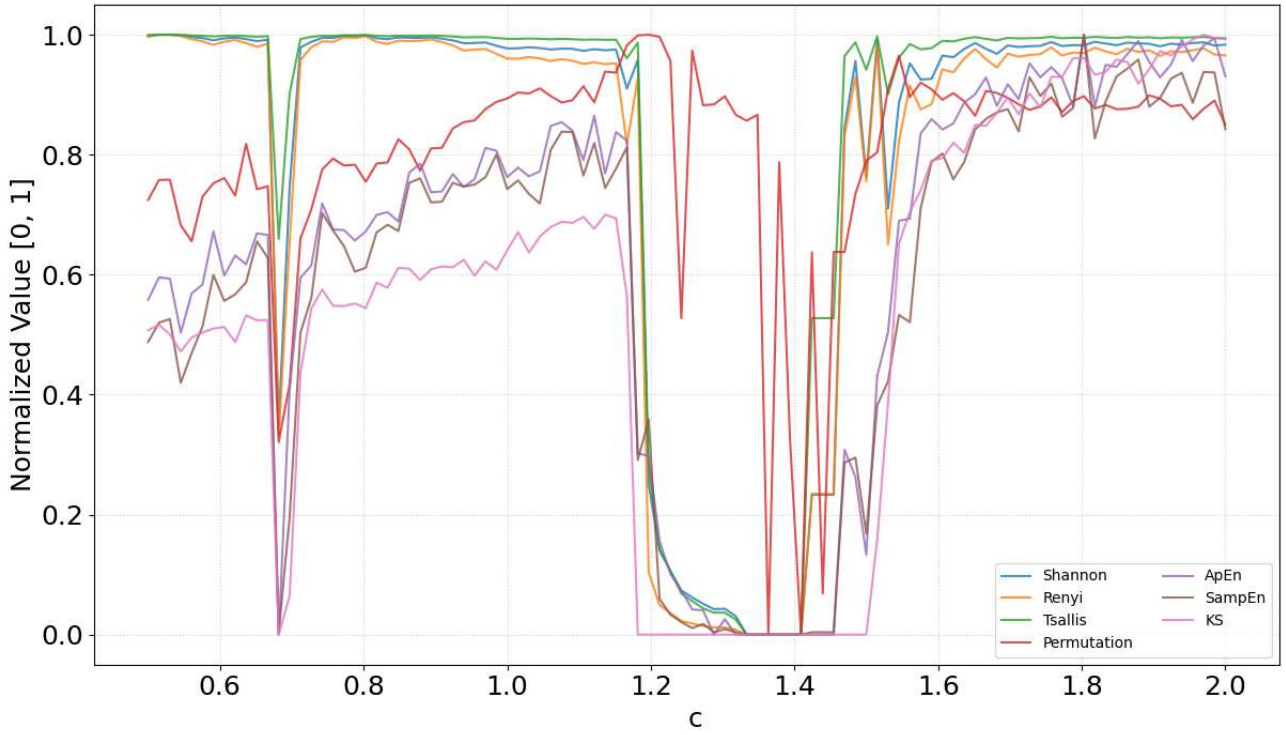


Figure 13: This figure shows normalized comparison of all seven entropy measures, where c is in $[0.5, 2.0]$ with fixed $a = 1.5$ and $b = -1.8$, and $d = 0.9$. The unified view confirms the high correlation between spatial complexity (Shannon) and temporal complexity (SampEn, PE). In regime $c \in [1.6, 2.0]$, all seven metrics converge toward their respective maxima, making this parameter space ideal for high-entropy sequence generation.

12 Multistability, Coexisting Attractors and Hysteresis Analysis

In this section, we investigate multistability through the coexistence of two or more stable attractors for a fixed set of parameters for the system (1). In nonlinear dynamical systems, multistability refers to the coexistence of two or more stable attractors for a fixed set of parameters [8]. This phenomenon is investigated using parameter continuation methods. We perform forward and backward sweeps of the control parameter c and detect hysteresis loops and coexisting invariant sets. It should be noted that forward period-doubling bifurcation sequences followed by reverse period-doubling sequences are not observed in all nonlinear dynamical systems. This phenomenon is one of the most common routes to chaos [3]. The fixed parameters are $a = 1.5, b = -1.8, d = 0.9$, while $c \in [1.0, 2.0]$. Two distinct bifurcation diagrams are constructed:

- **Forward Continuation (Blue)**: The parameter c is increased incrementally. For each step, the initial condition is set to the final state of the previous trajectory to ensure the system remains on the current branch of attractors in Fig. 14(A).
- **Backward Continuation (Red)**: The process is reversed, starting from $c = 2.0$ and decreasing to $c = 1.0$ shown in Fig.14(A).

In Fig. 14(B), there is a significant discrepancy between the two sweeps. A prominent hysteresis loop is observed in the region $c \in [1.8, 1.95]$. In the forward sweep, the system exhibits a sharp transition into a periodic window, whereas the backward sweep remains in a more diffused chaotic state or a different periodic attractor.

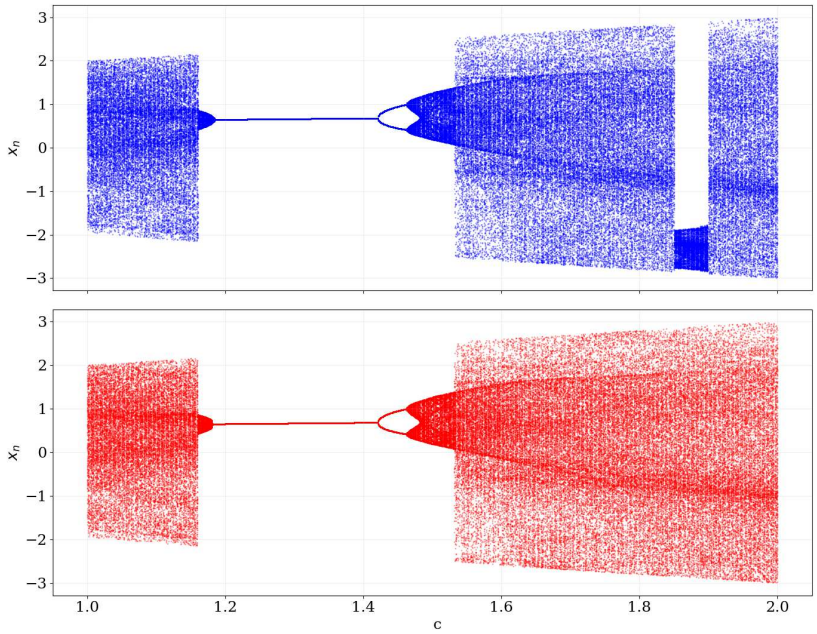
Coexisting Attractors and Basin Dependency

To verify multistability, we examine the system at a specific parameter value, $c = 1.549$, where the continuation sweeps show divergent mean behaviors. By initializing the map from two spatially separated points, initial conditions $\mathcal{IC}_A = (0.1, 0.1)$ and $\mathcal{IC}_B = (-2.5, 1.5)$, we successfully isolate two distinct coexisting attractors (Fig. 15).

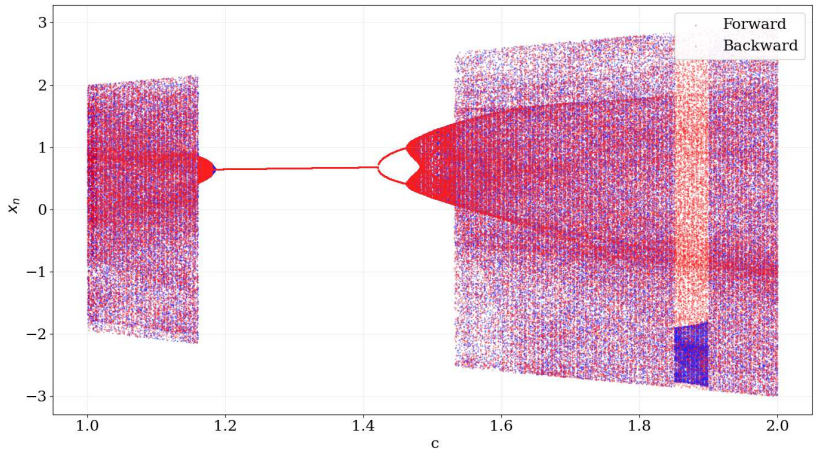
Dynamical Interpretation

The observed hysteresis suggests that the Clifford map undergoes subcritical bifurcations or crisis-induced transitions, where the destruction of one attractor does not necessarily imply the birth of the next in a continuous fashion. The fat fractal nature of the chaotic attractors further complicates the basin topology, leading to final state sensitivity even for small parameter perturbations.

The existence of multiple stable states has significant implications for applications in secure communication, as it allows for state-dependent signal modulation and increases complexity in the underlying chaotic carrier.



(A) Separated forward and backward continuations bifurcation diagram of the system (1) as the control parameter c is varied.



(B) Overleaped forward and backward continuations bifurcation diagram of the Clifford map as the control parameter c is varied.

Figure 14: This figure shows forward (blue) and backward (red) continuations bifurcation diagram. (A) The top panel displays the forward continuation obtained by incrementing c from $c_{\min} = 1.0$ to $c_{\max} = 2.0$ with fixed parameters $a = 1.5$, $b = -1.8$, and $d = 0.9$. The bottom panel shows the backward continuation obtained by decrementing c over the same range, starting from the final state of the forward sweep, using identical transient removal and sampling parameters. This highlights path dependence in the Clifford map and provides a clear diagnostic for parameter intervals where multiple attractors coexist. (B) This figure shows overlay of forward (blue) and backward (red) continuations to detect hysteresis region. This overlay emphasizes the presence of multistability and the practical importance of continuation direction when mapping the Clifford map's bifurcation structure.

13 Application

13.1 Clifford-Based Discrete Market Model

In this section, we present a Clifford-Based Discrete Market Model. It is a nonlinear framework for understanding financial price and sentiment dynamics. The trigonometric coupling in this model provides a robust mathematical proxy for the limits to arbitrage. By utilizing bounded sine and cosine functions, the model inherently respects the structural constraints of liquidity and volatility. We are using discrete mapping techniques to map the variables and parameters in economic terms. This shows the emergence of endogenous market volatility and the transition from stable equilibrium to chaotic crash regimes. This simulation reveals that as market sensitivity increases, the market model undergoes less volatility to extreme price deviations, and it also shows fluctuations in high-frequency trading intensity. These findings suggest that financial crises can be understood as endogenous phenomena driven by nonlinear feedback loops rather than purely exogenous stochastic shocks. The developed market model provides a theoretical formulation, numerical simulation results, and a detailed discussion of the implications for financial stability and risk management.

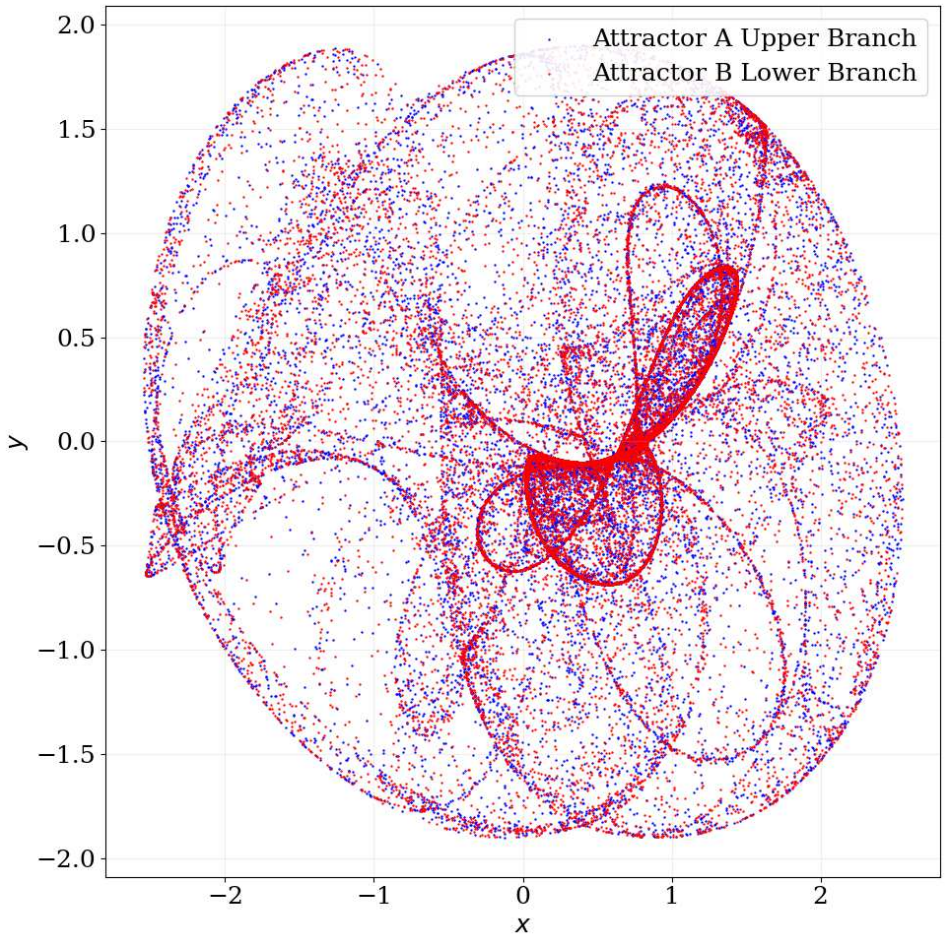


Figure 15: This figure shows coexisting attractors (Attractor A (blue) and Attractor B (red) coexist for the same parameter set) at the representative parameter value $c = 1.549$, where the other parameters are $a = 1.5$, $b = -1.8$ and $c = 1.549$, $d = 0.9$. Two widely separated initial conditions are $(x_0, y_0) = (0.1, 0.1)$ and $(x_0, y_0) = (-2.5, 1.5)$. This plot reveals the fine filamentary geometry and spatial separation of the two invariant sets where a blue colored set of points indicates upper branch (initial point $(0.1, 0.1)$) and a red colored set of points indicates lower branch (initial point $(-2.5, 1.5)$). Also, this plot provides direct phase-space evidence for multistability inferred from the continuation plots and demonstrates how different basins of attraction lead to qualitatively distinct long-term dynamics under identical parameter settings.

13.2 Theoretical Framework and Variable Mapping in Economics

We adapt this market model from the Clifford attractor map and define the evolution of the financial system through this nonlinear coupled system. The state of the market at any discrete time step $n + 1$ is determined by iterative mapping $\mathbf{f} : \mathbb{R}^2 \to \mathbb{R}^2$:

$$\begin{cases} x_{n+1} = \sin(a y_n) + c \cos(a x_n) \\ y_{n+1} = \sin(b x_n) + d \cos(b y_n), \end{cases}$$

where the state vector $S_n = (x_n, y_n)$ represents the endogenous coordinates of the market atmosphere. Unlike linear stochastic models, this deterministic framework captures the complex, non-periodic fluctuations, and regime switching characteristic of volatile asset classes.

We keep x_n as the logarithmic price deviation, which is the percentage deviation of the current market price from its underlying fundamental or fair value at the time step n. If $x_n > 0$, the asset is overvalued (speculative bubble phase). If $x_n < 0$, the asset is undervalued (oversold/depression phase). If $x_n = 0$, the market is in perfect fundamental equilibrium.

We keep y_n as the trading intensity (volume), which is a normalized measure of the aggregate energy or mood within the market, combining the trading volume with the bullish/bearish intensity. If $y_n > 0$, bullish sentiment dominates and high buying pressure is felt. If $y_n < 0$, bearish sentiment dominates and high selling pressure is felt. $|y_n|$ represents the total market kinetic Energy. The system's trajectory within the phase space is governed by the set of structural parameters $\boldsymbol{\theta} = \{a, b, c, d\}$, which characterizes the micro-foundations of the trader population: a denotes market sensitivity, b sentiment feedback, c systemic resilience, d trading inertia.

By this way, we map the dynamical system (1) to the Clifford based discrete market model. Now, in the upcoming sections, we perform the analysis of the market with respect to its defined parameters.

13.3 Market Sensitivity

To analyze the market's dynamical regimes, we perform the numerical simulations using the Clifford equations. We keep the following baseline values to represent a typical market structure.
Sentiment Feedback ($b = -1.8$), system resilience ($c = 1.6$), and trading inertia ($d = 0.9$). We treat parameter a as the primary control parameter that varies between key thresholds, $a = -0.1, 0.55, 0.56, 0.57, 0.58, 1.80$ to capture the evolution behavior of the system (1). We keep two primary visualizations (Phase Portrait and Bifurcation structure) to characterize the market model that highlights both stability and complexity.

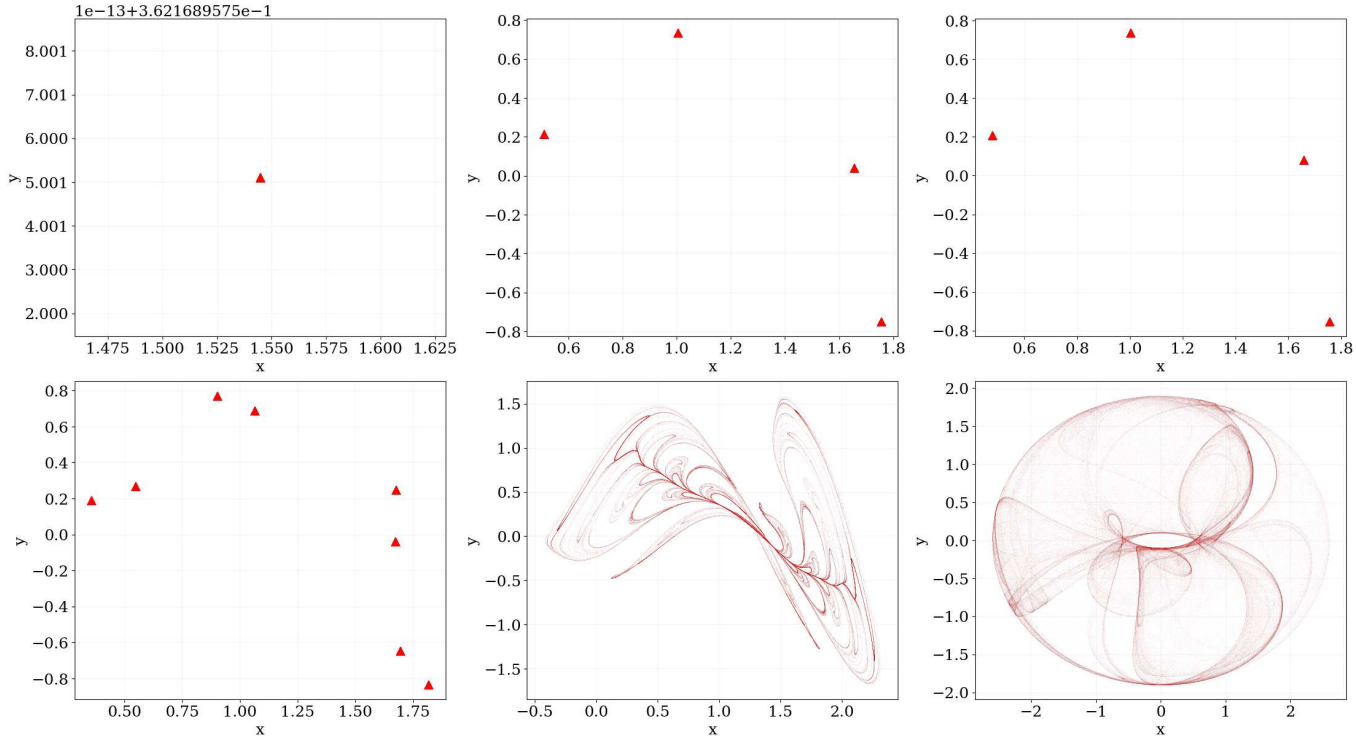


Figure 16: Plot of x against y to visualize the geometry of the market's long-term behavior, where left upper is showing the sable regime($a = -0.1$), cyclic volatility are shown by upper middle ($a = 0.55$), upper right ($a = 0.56$), and by left lower ($a = 0.57$). Lower middle ($a = 0.58$) and lower right ($a = 1.80$) show chaos to full chaos respectively.

13.3.1 Transition of Market Regimes

In Fig. 16, the results of the phase portrait simulations reveal three distinct qualitative regimes as the market sensitivity increases, which we can also observe in Fig. 17. In Figs. 16 and 17, with low sensitivity, we see that the market is in a stable phase or in a low-period orbit. In this case, price deviations and volatility (see Fig. 18) show a predictable equilibrium. Now, once a starts to increase, the system undergoes its first major bifurcation (as we can observe in Fig. 18). The stable phase is transformed into limit cycles of volatility or quasi-periodic orbits (refer to Fig.17). At high sensitivity, the system enters a chaotic state. The phase portrait transforms into a strange attractor, showing complex fractal-like structures (refer to Fig. 16). In this regime, price movements are irregular (as we can observe in Fig. 17), and the system exhibits a sensitive dependency. Even minor fluctuations in initial market sensitivity can lead to radically different price trajectories. Also, this dense region represents the market crash or crisis state (see Fig. 17). In this phase, price deviations reach their highest amplitudes, and the market exhibits extreme volatility. Importantly, this transition occurs without any change in the external environment.

13.4 Systemic Resilience

We analyze the market through systemic resilience and perform a rigorous sensitivity analysis. We fix the structural parameters as ($a = 1.5$, $b = -1.8$, and $d = 0.9$) and vary c from 1.25 to 2.0. We initialize the system $(x_0, y_0) = (0.1, 0.1)$, and the standard deviation (σ_x) of these points is calculated to measure the realized volatility.

In Fig. 19, the systemic resilience sensitivity of the Clifford based market model reveals three distinct structural impacts of c. Regime 1: when the market is in low Resilience ($c < 1.42$), the market is characterized by a Tight-Bound attractor. Because c is low, the cosine-based anchoring is weak, and the sine-based sentiment ($a \cdot y_n$) dominates, which results in relatively low-amplitude fluctuations in the market price deviation (see Fig. 19). Regime 2: as resilience increases ($1.42 < c < 1.55$), the attractor expands significantly. The bifurcation diagram (refer to Fig. 19) shows a characteristic widening of the steady-state cloud, mirroring transitions observed in volatility. Regime 3: beyond $c \approx 1.55$, the volatility curve (σ_x) increases linearly. This suggests that in a speculative market environment.

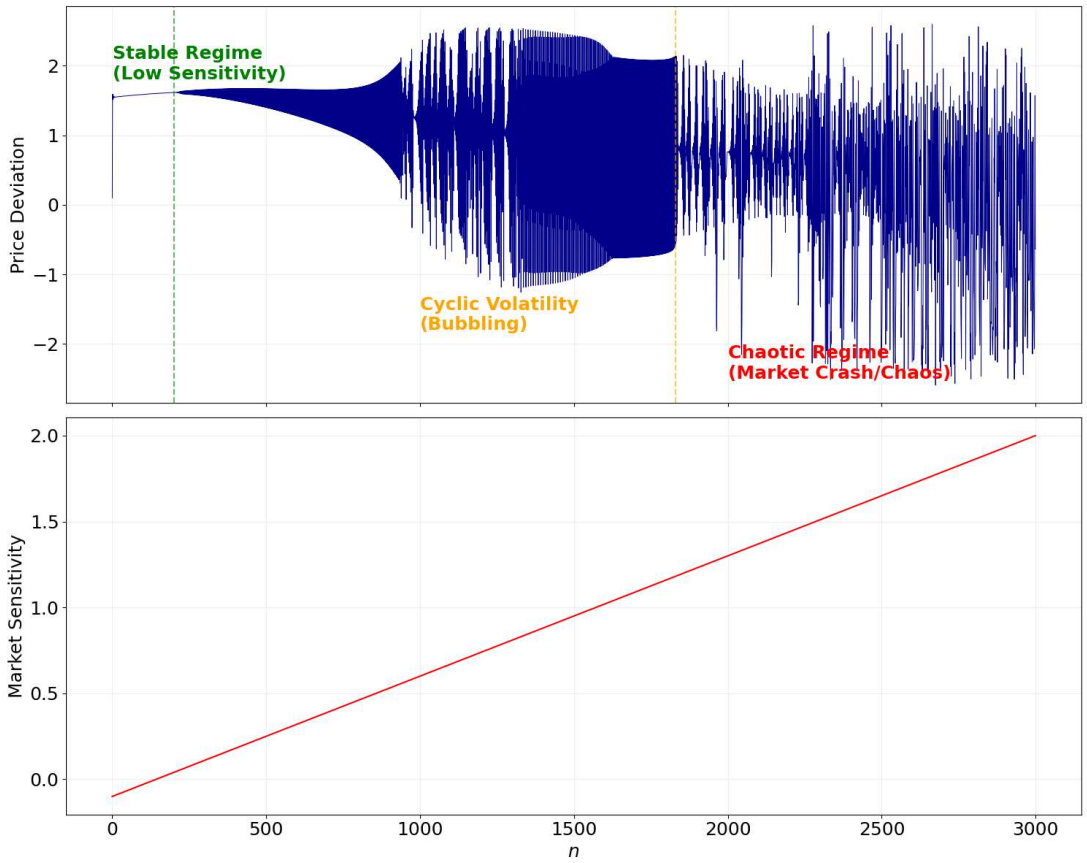


Figure 17: This plot shows time-series sweep of market sensitivity transition from stability to chaos. The top panel shows the simulated price deviation x_n while in bottom panel, the control parameter a is increased linearly from -0.1 to 2.0 over $n_{\text{steps}} = 3000$ iterations. The fixed parameters are $b = -1.8$ and $c = 1.6$, and $d = 0.9$ and the initial condition is $(x_0, y_0) = (0.1, 0.1)$. Vertical dashed lines and bold 18pt annotations mark qualitative regime boundaries used for interpretation. The stable regime (left, annotated near $n \approx 200$), the cyclic/periodic bubbling regime (middle, annotated near $n \approx 1830$), and the onset of chaotic crash dynamics (right, annotated beyond $n \gtrsim 2000$).

13.5 Global Volatility Surface

In Fig. 20, we keep fixed $b = -1.8$ and $d = 0.9$ and generate a three-dimensional surface plot mapping the realized volatility across a grid of Market Sensitivity (a) and Systemic Resilience (c) values to get a sense of the global structural stability of the Clifford based Market Model. We infer this as the global volatility surface. This surface reveals several important insights into market risk. At low sensitivity ($a < 0.5$), the market remains largely stable regardless of the resilience parameter (c), with volatility levels close to zero. As the sensitivity increases $a \geq 0.5$, we observe a sharp increase in volatility. This rise is amplified by higher values of c. The jagged nature of the surface in high-sensitivity regions indicates the presence of periodic windows in the market sense, the market briefly returns to a stable or periodic state before moving into high-amplitude chaos.

13.6 Sentiment Feedback

In this Clifford based discrete market model, the parameter b represents the feedback of the model. We keep fixed parameters $a = 1.5, c = -1.8, d = 0.9$ and varied $b \in [0, 2.0]$. In Fig. 21, the market remains stable for very low values of b ($b < 0.2$). As b increases, the volatility profile exhibits sharp peaks and the feedback loop between the price and sentiment feedback becomes highly unstable. This suggests that herding behavior is a major source of endogenous market volatility.

13.7 Trading Inertia

In the Clifford based discrete market model, trading inertia (parameter d) represents the persistence of the market over time. We keep fixed parameters $a = 1.5, b = -1.8, c = 1.6$, and vary $d \in [0, 2.0]$. The analysis of d (Fig. 22) shows that at low levels of $d < 1.1$, the market exhibits high-frequency oscillations, and beyond $d \approx 1.25$, volatility spikes again as inertia becomes too large, leading to sustained speculative bubbles.

13.8 Some other dynamical Indicators

In the Clifford based discrete market model, we can utilize several diagnostic metrics like Lyapunov exponents, Bifurcation diagrams, the $0-1$ Test, Entropies to as endogenous volatility, policy thresholds, information efficiency, determinism of crashes, respectively, to bridge the gap between abstract chaos and financial policy.

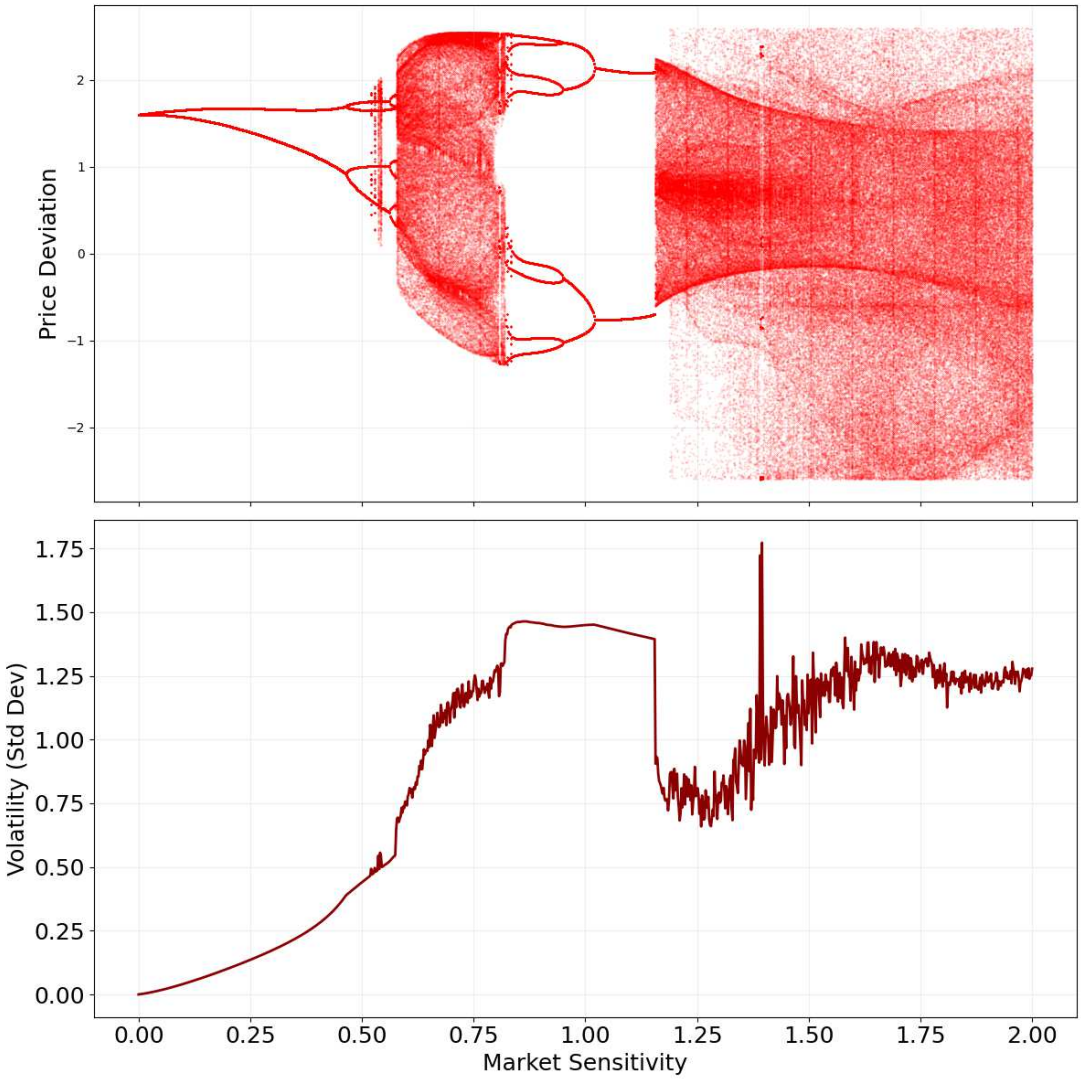


Figure 18: The top panel shows the bifurcation diagram obtained by plotting steady-state samples of the price deviation x against the control parameter a. The parameter a varies $a \in [0.0, 2.0]$, fixed parameters are $b = -1.8, c = 1.6,$ and $d = 0.9$, and initial condition is $(x_0, y_0) = (0.1, 0.1)$. The bottom panel plots the corresponding endogenous volatility, highlighting how volatility increases sharply near bifurcation thresholds and attains peak values in the chaotic regime.

14 Conclusions

In this paper, we have analyzed the dynamical behavior of the Clifford attractor. We have shown that the Clifford attractor exhibits a variety of rich dynamics, such as many fixed points with their stability, reverse doubling bifurcation, dissipative and non-dissipative fractal structures, multi-stability, coexistence, and various global bifurcations via one-to four-parameter bifurcation analysis. The bifurcation analysis provides a comprehensive characterization of Clifford's two-dimensional discrete system with trigonometric nonlinearities. By systematically varying the control parameter c while maintaining other parameters, we have identified multiple dynamical regimes, critical bifurcation points, period-doubling cascades, periodic windows, and crisis phenomena. The Lyapunov exponents have provided a clear quantitative explanation for the empty region in the bifurcation diagram. The $0-1$ test served as a crucial independent validator for the Lyapunov spectrum. Its ability to distinguish between bounded and diffusive behavior in translational variables provided clear evidence for the emergence of robust chaos as the control parameter c departs from the stable fixed-point regime. The comparative phase portraits provide visual confirmation of the dynamical transitions. In this study, we have presented the evolution from the Period-11 orbit to a dense strange attractor, serving as a qualitative bridge to quantitative diagnostics like Lyapunov exponents, the 0–1 tests, and the fractal dimension. As the control parameter c crosses the bifurcation threshold, the basin of attraction evolves from a simple, smooth manifold into a complex, fractal-like structure. By the Kaplan-Yorke conjecture, it has been confirmed that the Clifford system demonstrates high versatility, manifesting itself either as a delicate fractal set ($D \approx 1.29$) or as a robust attractor that fills the 2D plane. The emergence of $D = 2.0$ chaotic attractors in Clifford-type maps highlights the nonlinear mixing capabilities of the system, and the transition from $D < 2$ to $D = 2$ represents a critical topological shift. This duality allows the Clifford map to serve as a bridge between the study of delicate fractal measures and the theory of space-filling chaotic measures. Also, the multi-entropy framework has provided a comprehensive toolkit for characterizing similar discrete-time dynamical systems across diverse scientific applications. This research has also successfully demonstrated that the Clifford-Based Discrete Market Model offers a powerful alternative to stochastic finance models to identify the structural roots of market instability. The generated

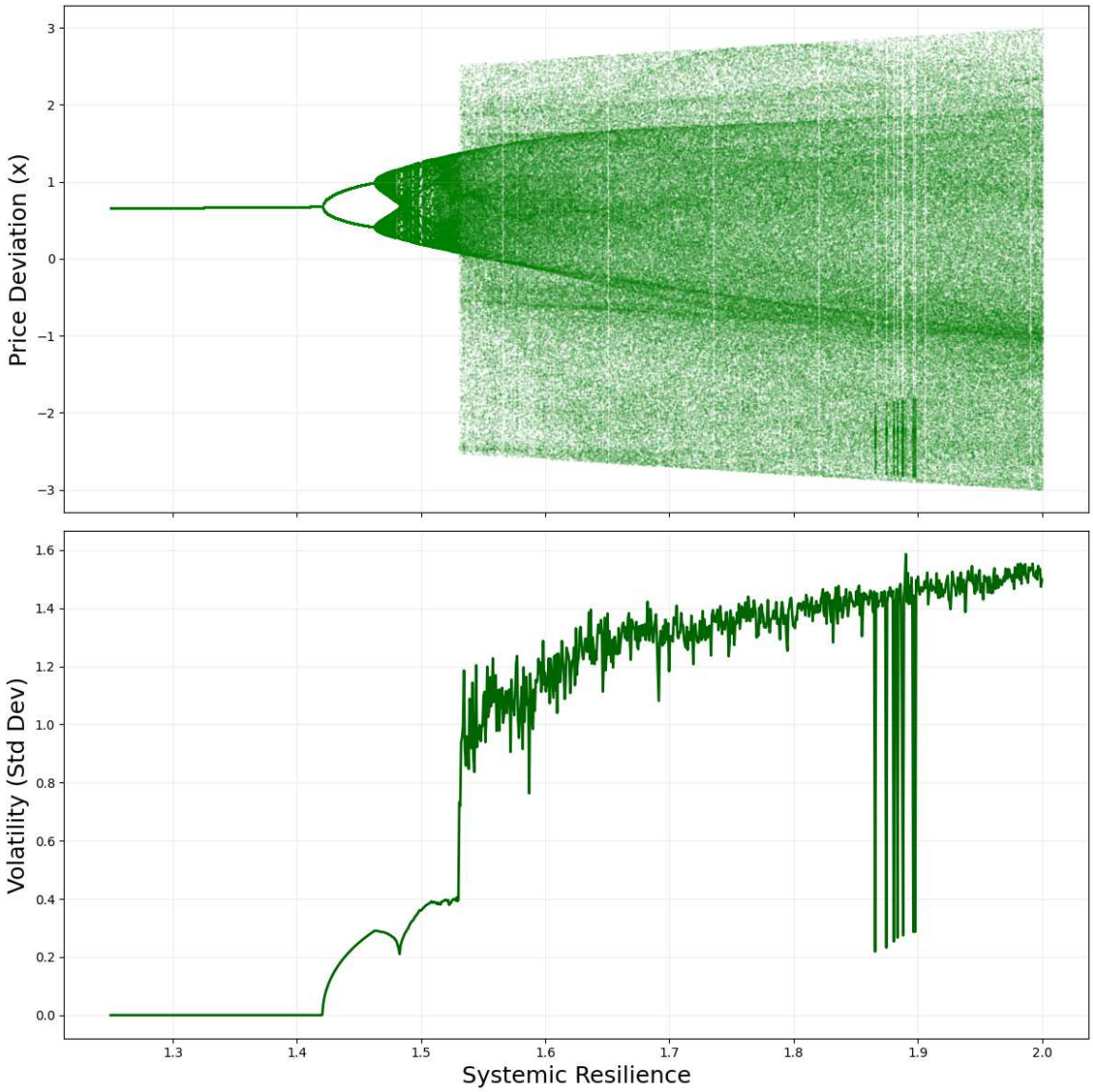


Figure 19: This figure shows the bifurcation and volatility profiles for variable Systemic Resilience (c). The top figure shows the steady-state spread of price deviation and the bottom figure shows the corresponding standard deviation (volatility). The fixed parameters are $a = 1.5$ and $b = -1.8$, and $d = 0.9$. The initial condition is $(x_0, y_0) = (0.1, 0.1)$.

phase portraits and bifurcation diagrams serve as a quantitative red line for regulators, identifying the exact transition points between stable growth, cyclic bubbling, and chaotic collapse.

Acknowledgements

Our heartfelt gratitude goes to Professor Clifford A. Pickover, whose extraordinary dedication and remarkably detailed critique provided invaluable guidance. His overwhelming depth of review and thoughtful suggestions have left a lasting imprint on this research.

Funding

The fourth author acknowledges the support of the Anusandhan National Research Foundation (ANRF), Ministry of Education India, under Grant No. ANRF/ARG/2025/004946/MS.

Declaration of Competing Interest

The authors declare that they have no competing interests related to the publication of this article.

Data Availability

No data were generated or analyzed in this study.

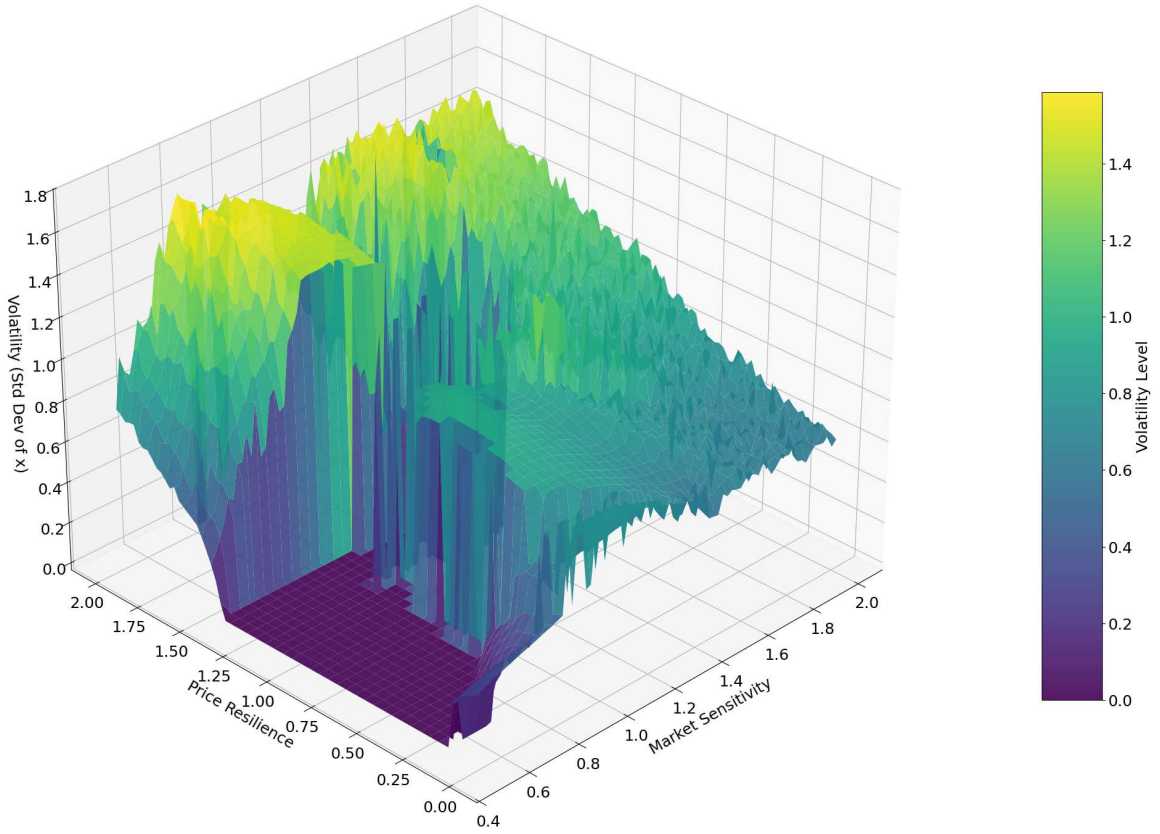


Figure 20: This figure shows Global Volatility Surface (a, c). The surface reveals a significant expansion of market volatility when high sensitivity ($a > 1.25$) combined with high resilience ($c > 1.55$). The surface maps the realized endogenous volatility (standard deviation of x in steady state) across a uniform grid with $a \in [0.5, 2.0]$ and $c \in [0.0, 2.0]$. The fixed parameters are $b = -1.8$ and $d = 0.9$. Figure exhibits followings: (1) a Stability Plateau at low sensitivity ($a \lesssim 0.5$) where volatility remains near zero across c; (2) a pronounced Resonance Ridge where volatility rises sharply as a increases and is amplified by larger c; (3) The high sensitivity ($a \gtrsim 1.25$) combined with high resilience ($c \gtrsim 1.55$) produces unexpectedly large volatility peaks; and (4) jagged Chaotic Valleys and narrow periodic windows in high-sensitivity regimes that indicate band-merging and local returns to periodicity.

Declaration Statement

The authors acknowledge the use of AI-based tools to assist in improving the language, clarity, and presentation of the manuscript. All intellectual content, technical contributions, and final interpretations were developed, verified, and approved by the authors.

References

[1] Azzaby F. E., Akkad N. E., Sabour K., sishushankarmuni@gmail.comKabbaj S. An RGB image encryption algorithm based on Clifford attractors with a bilinear transformation. International Conference On Big Data and Internet of Things (116-127), Cham: Springer International Publishing (2021).

[2] Bandt, C., Pompe, B. Permutation entropy: A natural complexity measure for time series. Physical Review Letters, 88(17), 174102 (2002).

[3] Bayani, A., Rajagopal, K., Khalaf, A. J. M., Jafari, S., Leutcho, G. D., Kengne, J. Dynamical analysis of a new multistable chaotic system with hidden attractor: Antimonotonicity, coexisting multiple attractors, and offset boosting. Physics Letters A, 383(13), 1450-1456 (2019).

[4] Bensaid, M., Hamdi, M. (2019). Secure communication systems based on the synchronization of chaotic systems. In Advances in Intelligent Systems and Computing, 915, 123-135, Springer (2019).

[5] Daza A, Wagemakers A, Georgeot B, Guéry-Odelin D, Sanjuán MA. Basin entropy: a new tool to analyze uncertainty in dynamical systems. Scientific reports. 6(1):31416 (2016).

[6] Elaydi, Saber N. Discrete chaos: with applications in science and engineering. Chapman and Hall/CRC, 2007.

[7] Fatoyinbo, H. O., Muni, S. S., Ghosh, I., Sarumi, I. O., Abidemi, A. Numerical Bifurcation Analysis of Improved Denatured Morris-Lecar Neuron Model. International Conference on Decision Aid Sciences and Applications (DASA), 1-6, IEEE (2022).

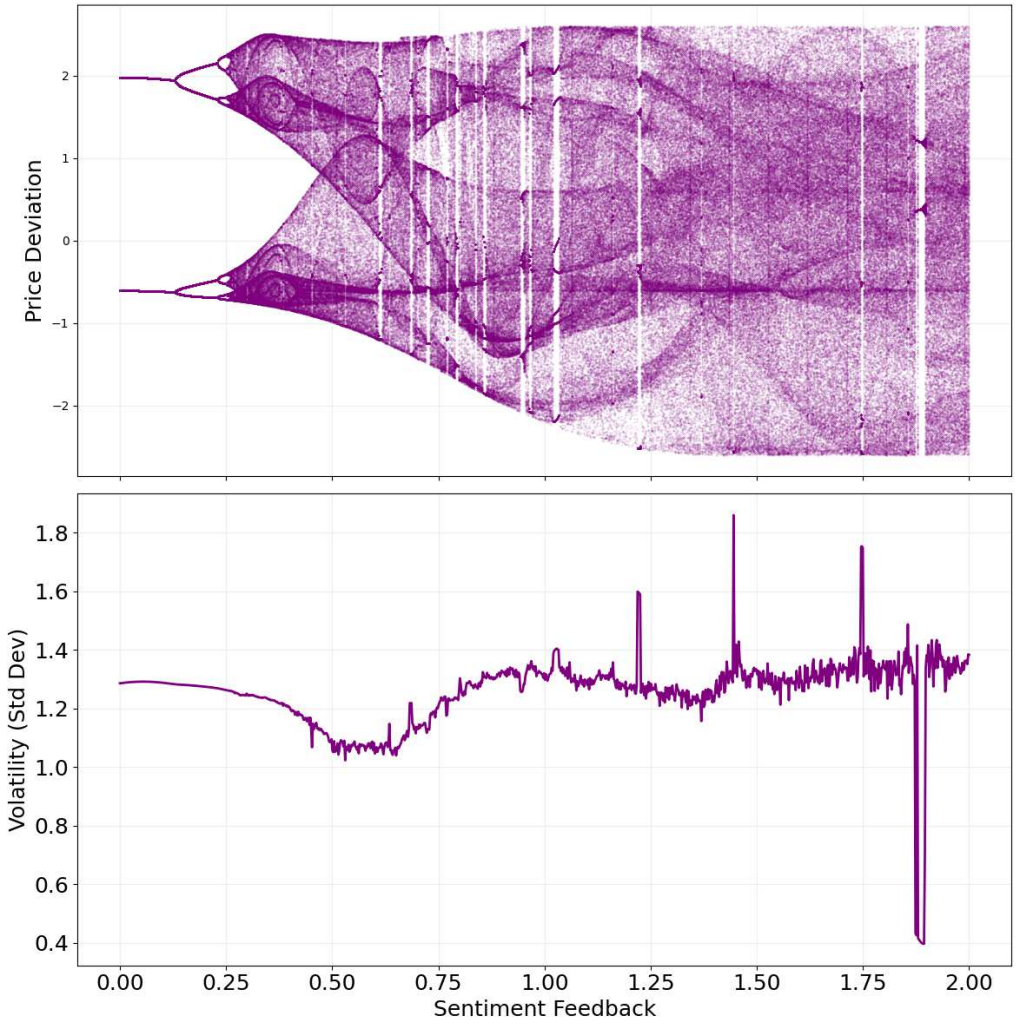


Figure 21: This figure shows the impact of Sentiment Feedback (b). Top: Bifurcation diagram showing the route to chaos. Bottom: Market Volatility profile with respect to the sentiment feedback(b). The fixed parameters are $a = 1.5$ and $c = 1.6$, and $d = 0.9$ and b is varied over the interval $[0, 2.0]$. The initial condition is $(x_0, y_0) = (0.1, 0.1)$.

[8] Feudel U. Complex dynamics in multistable systems. International Journal of Bifurcation and Chaos. 18(06):1607-26 (2008).

[9] Gao, Y., Liu, B. Study on the dynamical behaviors of a two-dimensional discrete system. Nonlinear Analysis: Theory, Methods Applications, 70(12), 4209–4216 (2009).

[10] Gottwald, G. A., Melbourne, I. A new test for chaos in deterministic systems. Proceedings of the Royal Society of London. Series A, 460(2042), 603–611 (2004).

[11] Gottwald, G.A., Melbourne, I. On the implementation of the 0–1 test for chaos. SIAM Journal on Applied Dynamical Systems, 8(1), 129–145 (2009).

[12] Grassberger P, Procaccia I. Characterization of strange attractors. Physical review letters. 50(5):346 (1983).

[13] Grassberger P, Procaccia I. Measuring the strangeness of strange attractors. Physica D: nonlinear phenomena. 9(1-2):189-208 (1983).

[14] Greene, J. M. Kim, J. S. The calculation of Lyapunov spectra. Physica D: Nonlinear Phenomena, 24(1-3), 213-225 (1987).

[15] Güvenoglu, E. An image encryption algorithm based on multi-layered chaotic maps and its security analysis. Chaos, Solitons Fractals, 178, 114345 (2024).

[16] Ivanova T, Stoyanov B, Dobrev D. Secure text encryption based on clifford attractors. In2023 31st National conference with international participation (TELECOM), 1-4, IEEE (2023).

[17] Kanafchian M, Fathi-Vajargah B. A novel image encryption scheme based on clifford attractor and noisy logistic map for secure transferring images in navy. International Journal of e-Navigation and Maritime Economy. 6:53-63 (2017).

[18] Kaplan J. L., Yorke J. A. Chaotic behavior of multidimensional difference equations. InFunctional Differential Equations and Approximation of Fixed Points: Proceedings, Bonn, 204-227, Berlin, Heidelberg: Springer Berlin Heidelberg (2006).

[19] Kuznetsov S. P., Kuznetsov A. P., Sataev I. R. Multiparameter critical situations, universality and scaling in two-dimensional period-doubling maps. Journal of Statistical Physics. 121(5):697-748 (2005).

[20] Lakshminarayan, A., Tomsovic, S. Chaos and the quantum-classical correspondence in the kicked pendulum. Physical Review E, 64(3), 036207 (2011).

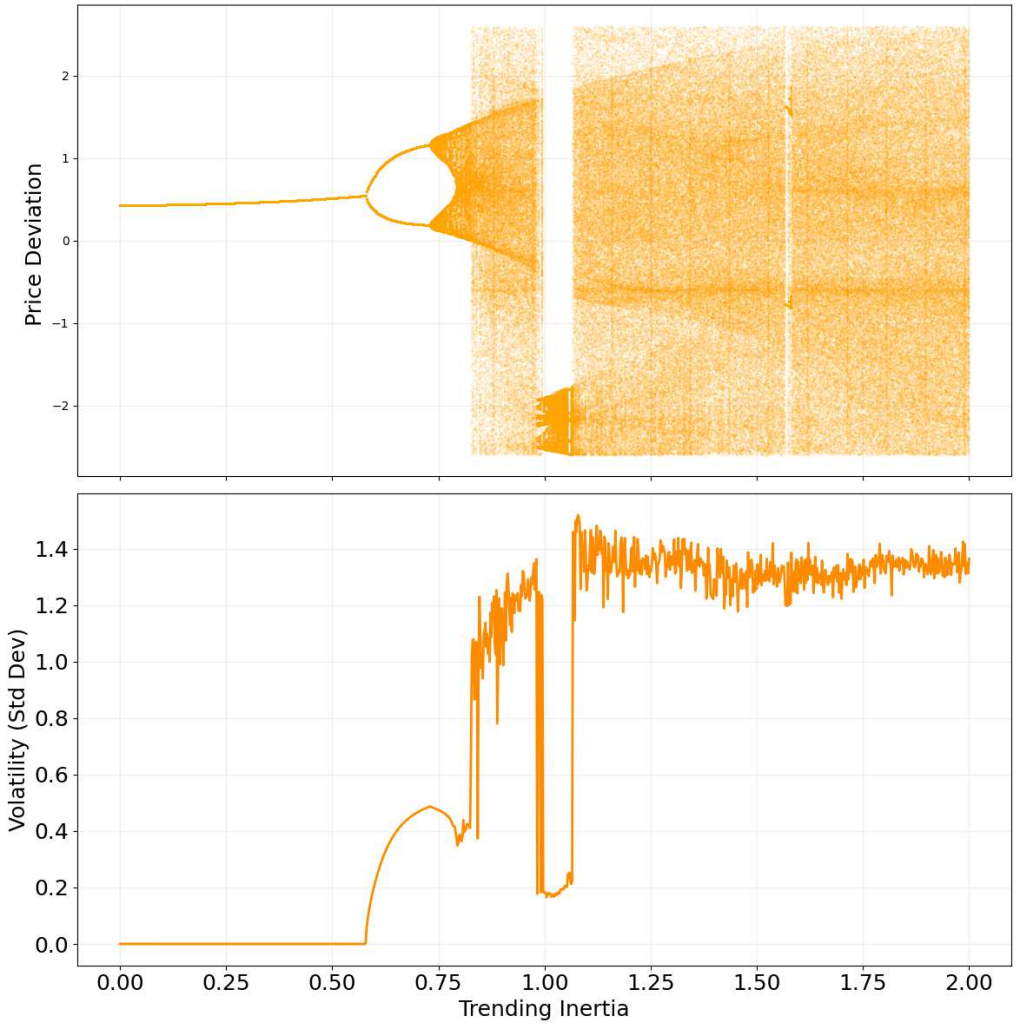


Figure 22: This figure shows the impact of the Sentiment Inertia (d). Top figure shows the bifurcation diagram and bottom figure shows volatility profile. The fixed parameters are $a = 1.5$ and $c = 1.6$, and $b = -1.8$ and d is varied over the interval $[0, 2.0]$. The initial condition is $(x_0, y_0) = (0.1, 0.1)$.

[21] Arroyo D, Alvarez G, Li S, Li C, Fernandez V. Cryptanalysis of a new chaotic cryptosystem based on ergodicity. International Journal of Modern Physics B. 23(05):651-9 (2009).

[22] Makarkin, S.Y., Koronovskii, A.A., Hramov, A.E., Shurygina, S.A. Permutation entropy as a universal measure of complexity in spatially extended systems. Technical Physics Letters, 43(9), 839-842 (2017).

[23] Muni SS, Fatoyinbo HO, Ghosh I. Dynamical effects of electromagnetic flux on chialvo neuron map: nodal and network behaviors. International Journal of Bifurcation and Chaos. 32(09):2230020 (2022).

[24] Nardo LG, Nepomuceno EG, Arias-Garcia J, Butusov DN. Image encryption using finite-precision error. Chaos, Solitons Fractals. (2019).

[25] Hartl MD. Lyapunov exponents in constrained and unconstrained ordinary differential equations. arXiv preprint physics/0303077. 2003.

[26] Ott E. Chaos in dynamical systems. Cambridge university press; (2002).

[27] Pesin, Y.B. Characteristic Lyapunov exponents and smooth ergodic theory. Russian mathematical surveys, 32(4), 55-114 (1977).

[28] Pickover, C.A. Chaos in wonderland: visual adventures in a fractal world. St. Martin's Press, Inc. (1995).

[29] Pincus, S.M. Approximate entropy as a measure of system complexity. Proceedings of the national academy of sciences, 88(6), 2297–2301 (1991).

[30] Richman, J.S., Moorman, J.R. Physiological time-series analysis using approximate entropy and sample entropy. American journal of physiology-heart and circulatory physiology, 278(6), H2039-H2049 (2000).

[31] Rényi, A. On measures of entropy and information. In Proceedings of the fourth Berkeley symposium on mathematical statistics and probability, volume 1: contributions to the theory of statistics (Vol. 4, pp. 547-562). University of California Press (1961).

[32] Shannon, C.E. A mathematical theory of communication. The Bell system technical journal, 27(3), 379–423 (1948).

[33] Strogatz, S.H. Nonlinear dynamics and chaos: with applications to physics, biology, chemistry, and engineering. Chapman and Hall/CRC (2024).

[34] Thompson, J.M.T., Stewart, H.B. (2002). Nonlinear Dynamics and Chaos. John Wiley & Sons.

[35] Tsallis, C. Possible generalization of Boltzmann-Gibbs statistics. Journal of statistical physics, 52(1), 479–487 (1988).

[36] Ueda, Y. Steady motions exhibited by Duffing's equation-a picture book of regular and chaotic motions. Research Report: IPPJ (1980).

[37] Wang, K., Pei, W., Xia, H., Cheung, Y.M. Pseudo-random number generator based on asymptotic deterministic randomness. Physics Letters A, 372(24), 4388–4394 (2008).

[38] Wolf, A., Swift, J.B., Swinney, H.L. and Vastano, J.A. Determining Lyapunov exponents from a time series. Physica D: nonlinear phenomena, 16(3), 285–317 (1985).

A Appendix

This appendix provides the reproducible computational framework used to derive the dynamical properties of the Clifford system. All implementations are written in Python 3.10+ utilizing the `NumPy` and `SciPy` libraries. You can access the Python code on the GitHub link:
https://github.com/Shubham11106/Clifford-Attractor-Reproducible-code.git.